Properties of Ca^{2+} sparks revealed by four-dimensional confocal imaging of cardiac muscle

Vyacheslav M. Shkryl, Lothar A. Blatter, and Eduardo Ríos

Department of Molecular Biophysics and Physiology, Section of Cellular Signaling, Rush University, Chicago, IL 60612

Parameters (amplitude, width, kinetics) of Ca^{2+} sparks imaged confocally are affected by errors when the spark source is not in focus. To identify sparks that were in focus, we used fast scanning (LSM 5 LIVE; Carl Zeiss) combined with fast piezoelectric focusing to acquire *x*–*y* images in three planes at 1-µm separation (*x*-*y*-*z*-*t* mode). In 3,000 *x*–*y* scans in each of 34 membrane-permeabilized cat atrial cardiomyocytes, 6,906 sparks were detected. 767 sparks were in focus. They had greater amplitude, but their spatial width and rise time were similar compared with all sparks recorded. Their distribution of amplitudes had a mode at $\Delta F/F_0 = 0.7$. The Ca^{2+} release current underlying in-focus sparks was 11 pA, requiring 20 to 30 open channels, a number at the high end of earlier estimates. Spark frequency was greater than in earlier imaging studies of permeabilized ventricular cells, suggesting a greater susceptibility to excitation, which could have functional relevance for atrial cells. Ca^{2+} release flux peaked earlier than the time of peak fluorescence and then decayed, consistent with significant sarcoplasmic reticulum (SR) depletion. The evolution of fluorescence and release flux were strikingly similar for in-focus sparks of different rise time (*T*). Spark termination involves both depletion of Ca^{2+} in the SR and channel closure, which may be synchronized by depletion. The observation of similar flux in sparks of different *T* requires either that channel closure and other termination processes be independent of the determinants of flux (including $[Ca^{2+}]_{SR}$) or that different channel clusters respond to $[Ca^{2+}]_{SR}$ with different sensitivity.

The Journal of General Physiology

INTRODUCTION

In striated muscles, action potentials cause intracellular Ca^{2+} channels to open, and the ensuing Ca^{2+} release initiates contraction. In cardiac muscle and in skeletal muscle of some taxonomic classes, Ca^{2+} release is composed of discrete events from SR Ca^{2+} channels (RyRs) of fairly stereotypical appearance, which have been visualized with confocal fluorescence microscopy and fluorescent Ca^{2+}-sensitive dyes, and termed "Ca^{2+} sparks" (Cheng et al., 1993; Nelson et al., 1995; Tsugorka et al., 1995). Ca^{2+} sparks are a collective phenomenon produced by a group of mutually interacting RyR channels within a couplon (Stern et al., 1997, 1999), defined as the release channels in a cluster or Ca^{2+} release unit (Franzini-Armstrong and Jorgensen, 1994) together with its associated L-type Ca^{2+} channels and/or voltage sensors. Ca^{2+} sparks occur in ventricular (Niggli and Shirokova, 2007) as well as in atrial myocytes (e.g., Blatter et al., 1997; Kockskämper et al., 2001; Sheehan et al., 2006). In ventricular myocytes, the well-developed 3-D network of transverse (t) tubules (Soeller and Cannell, 1999) ensures that in response to an action potential, all couplons are activated synchronously, which results in a highly uniform Ca^{2+} release throughout the entire cell volume (Cheng et al., 1994). In contrast, in atrial myocytes, the t-tubular network is poorly developed or entirely absent (Hüser et al., 1996; Cordeiro et al., 2001; Mackenzie et al., 2001), and close apposition of surface membrane Ca^{2+} channels and RyRs only exists in the cell periphery. The SR, however, extends throughout the entire cell and contains RyRs capable of Ca^{2+} release and generation of Ca^{2+} sparks (Sheehan et al., 2006). Although sparks appear to require the phenomenon of CICR (Endo et al., 1970; Fabiato and Fabiato, 1978; Cheng et al., 1993; Klein et al., 1996) for both initiation and propagation within the channel cluster, many other mechanistic details of these events remain unknown or poorly understood. Thus, numbers of channels involved, time course of their unitary current, duration of opening of the individual channels within a couplon, the mechanisms underlying their closure, the degree of local intra-SR depletion, and even the behavior of channels and currents at the time when the spark peaks have remained uncertain or are just starting to be elucidated.

Many of these unknowns could be eliminated by an accurate quantification of sparks, in terms of their so-called morphometric parameters. These include peak amplitude, spatial width (or full width at half maximum

Correspondence to Eduardo Ríos: erios@rush.edu

V.M. Shkryl's present address is Dept. of General Physiology of the Nervous System, A.A. Bogomoletz Institute of Physiology, 01024 Kiev, Ukraine.

Abbreviations used in this paper: DHPR, dihydropyridine receptor; ecc, excitation–contraction coupling; FWHM, full width at half maximum; nj-SR, nonjunctional SR.

The Rockefeller University Press $30.00
J. Gen. Physiol. Vol. 139 No. 3 189–207
www.jgp.org/cgi/doi/10.1085/jgp.201110709

[FWHM]), rise time, decay time constant and other measures of duration, and integral evaluations of intensity or signal mass (ZhuGe et al., 2000; Chandler et al., 2003). For instance, the local amplitude of the change in [Ca^{2+}] together with knowledge of the unitary channel current will provide an indication of the number of channels open. Similar insights will be derived from the accurate knowledge of spatial width. In this regard, a combination of modeling and experimental testing have shown that spatial width of sparks grows with the time that the release channels remain open (Zhou et al., 2003), but widths that reach values beyond certain limits at early times, for example in "protoplatykurtic" sparks (Zhou et al., 2005), reflect spatially large sources rather than small groups of channels. Finally, detailed knowledge of spatial aspects of sparks and their evolution in time can be used to reconstruct the underlying release current by different methods that yield mutually consistent results (see Ríos et al., 1999, and Soeller and Cannell, 2002, for alternative methods, named "backward" and "forward" to distinguish whether the effect [the change in [Ca^{2+}]] or the cause [the release current] is the starting point of the calculation). An accurate morphometry of sparks is therefore essential for the elucidation of their control mechanisms.

Crucial determinants of control of Ca^{2+} sparks are believed to depend on cytosolic Ca^{2+} itself, including complementary mechanisms of activation (CICR) and inactivation (Ca^{2+}-dependent inactivation; Sham et al., 1998, for cardiac; Baylor et al., 1983, and Melzer et al., 1984, for skeletal). These result in channels that do not open or close independently but gate concertedly. Whether or not channels gate independently changes another morphometric property, the distribution of spark amplitudes, which will be a sum of decaying exponential functions of amplitude if arising from openings of individual channels that are mutually independent (and are "Markovian" or memoryless, e.g., Colquhoun and Hawkes, 1983; see also http://en.wikipedia.org/wiki/Markov_process for a brief definition), but will typically have a mode or preferred amplitude if channels gate concertedly (Bridge et al., 1999; Cannell and Soeller, 1999; Ríos et al., 2001; Wang et al., 2002). For instance, it has been argued that the rise time characteristics are incompatible with the idea that a spark arises from a single RyR channel with a reversible Markovian gating scheme (Shirokova et al., 1999; Ríos et al., 2001; Wang et al., 2002). On the other hand the spark amplitude experimentally recorded in line-scan mode always obeys a monotonically decaying distribution, regardless of the true spark amplitude (Cheng et al., 1999; Ríos et al., 2001).

A major obstacle to reaching the desired accuracy in measures of spark parameters is that measurements are done on confocal images, including line scans (*x*–*t*, herein called 2-D) and *x*–*y* scans (referred to as 3-D imaging). In either case, sparks are imaged without knowledge of the location of its originating couplon relative to the line or plane of scanning. Starting with the work of Pratusevich and Balke (1996), it has become increasingly clear that all morphometric spark parameters are affected by the out-of-focus error. Out-of-focus errors include reduced amplitude, increased spatial spreading, and slower kinetics. Among the parameters, amplitude is most affected, decaying sharply with distance from source to scanning line or plane, whereas rise time and FWHM are less distorted (Pratusevich and Balke, 1996; Smith et al., 1998). It is because of this susceptibility to focus error that the distribution of amplitudes of sparks detected in line scans must be monotonously decreasing.

Theoretical approaches have been developed to recover the true spark amplitude, allowing quantitative corrections of spark amplitudes as if all sparks would have been in focus (Shirokova and Ríos, 1997; Izu et al., 1998; Ríos et al., 2001). Specifically Ríos et al. (2001) provide an equation to derive the distribution of true amplitudes from the distribution histogram of measured amplitudes.

Although these procedures have value, as they demonstrated, for example, a mode in the distribution of true amplitudes, consistent with expectations for groups of nonindependent channels, the correction formula has not been verified. Moreover, it requires knowledge of other parameters, which are also affected by the out-of-focus error and therefore are not knowable with certainty.

Here, we take advantage of two novel tools, the fast *x*–*y* scanning provided by a slit confocal scanner (LSM 5 LIVE; Carl Zeiss) and the ability to move the plane of focus vertically in rapid and reproducible manner to achieve *x*-*y*-*z*-*t* (or 4-D) imaging of sparks. 4-D scanning eliminates the out-of-focus error because it allows identification of sparks that are imaged in focus. In this way, we characterize morphometrically a large group of sparks in focus. We use these, for the first time well-determined measures, to both clarify aspects of control of Ca^{2+} release and produce a strict test of the theory of scanning in lower dimensions.

Part of this work has been presented in abstract form (Shkryl, V.M., and L.A. Blatter. 2008. Biophysical Society 52nd Annual Meeting. Abstr. 495; Shkryl, V.M., and L.A. Blatter. 2009. Biophysical Society 53rd Annual Meeting. Abstr. 1415; Shkryl et al. 2011. Biophysical Society 55th Annual Meeting. Abstr. 3032).

MATERIALS AND METHODS

Cell isolation and solutions

Single myocytes were isolated from cat atria as described previously (Wu et al., 1991; Kockskämper and Blatter, 2002; Sheehan and Blatter, 2003). The procedure for cell isolation was fully approved by the Institutional Animal Care and Use Committee. In brief, adult mongrel cats of either sex were anesthetized with sodium pentobarbital (50 mg kg^{-1}). After thoracotomy, hearts

were quickly excised, mounted on a Langendorff apparatus, and retrogradely perfused with oxygenated collagenase–containing solution at 37°C. Myocytes were used 1–6 h after isolation. Freshly isolated myocytes were plated on glass coverslips in normal Tyrode's solution (composition in mM: 135 NaCl, 4 KCl, 2 $CaCl_2$, 1 $MgCl_2$, 10 D-glucose, and 10 HEPES, with pH adjusted to 7.4 with NaOH).

Imaging of Ca^{2+} sparks was performed in cells permeabilized with saponin (0.005%) for 40 s (Zima et al., 2003) in an internal solution composed of (in mM): 120 potassium aspartate, 15 KCl, 5 KH_2PO_4, 5 MgATP, 0.35 EGTA, 0.14 $CaCl_2$, 0.75 $MgCl_2$, 10 phosphocreatine sodium salt, 4% dextran, and 10 HEPES, with pH adjusted to 7.2 with KOH. Subsequently, the bath solution was exchanged to a saponin-free internal solution containing 40 µM fluo-4 pentapotassium salt (Invitrogen). The free [Ca^{2+}] and [Mg^{2+}] of this solution were 100 nM and 1 mM, respectively. All experiments were performed at room temperature (22–24°C). Chemicals were purchased from Sigma-Aldrich.

Fluo-4 was excited at 488 nm, and emission was collected at >520 nm. The cell was positioned with its long axis parallel to the *x* scanning direction (which in slit scanners is acquired simultaneously at all points of a 512-pixel line).

4-D confocal image acquisition and multidimensional analysis of sparks

Fluorescence image acquisition was performed on a slit scanning confocal microscope (LSM 5 LIVE; Carl Zeiss) equipped with a 63×, 1.20 n.a. water-immersion objective (C-Apochromat; Carl Zeiss) and a piezoelectric focusing attachment, which by moving the objective allowed us to collect three *x*–*y* images (512 × 31 pixels; pixel distance of 0.42 µm) in succession, separated by 1 µm in the vertical (*z*) direction. The point-spread function of the system with the focusing attachment had FWHM values of 0.52, 0.46, and 1.25 µm, respectively, in the *x*, *y*, and *z* directions. The scan time for an individual image was 1.16 ms (line dwell time of 15.7 µs), and the acquisition time for one trio of images was 5.6 ms (Fig. 1 A; note that the acquisition time for a trio is longer than the sum of scan times for three images because of the time required for scanner fly back and movement of the piezoelectric focusing attachment). A total of 1,000 trios, or 3,000 *x*–*y* images, were acquired for each cell at the same location. To refer to such series of images we will use interchangeably the terms "*x*-*y*-*z*-*t* series" and "4-D series." We will refer to series at a single *z* position as "*x*-*y*-*t*" or "3-D series." Similarly, "*x*–*t* series" will be also called "2-D" or line scans.

Images in 4-D and 3-D series were normalized to resting fluorescence by a procedure in which individual images $F(x,y)$ are divided pixel by pixel by a normalizing image $F_0(x,y)$ constructed by averaging every image with spark regions blanked. The set of blanked images was also used to compute a bleaching correction function (see Brum et al., 2000, for details).

Sparks were detected automatically in normalized, bleach-corrected *x*-*y*-*t* series using the algorithm developed by Brum et al. (2000), which is an adaptation to 3-D scans of the procedure introduced for line scans (Cheng et al., 1999). The procedure identifies the location coordinates of the center of mass of each spark, a maximum of $\Delta F/F_0$ (where $\Delta F = F - F_0$) in each image, a subseries of consecutive images recognized as corresponding to the same spark and a peak of the maximum of $\Delta F/F_0$ within the subseries, which we refer to as peak amplitude or just amplitude (a). The analysis also produced for each spark a time of first detection, an interval between first detection and the attainment of peak amplitude (rise time, T), plus several measures of the spatial properties, including width in *x* and *y*, and eccentricity.

For this study, we specifically developed a definition and automatic determination of FWHM. We defined FWHM as the diameter of a circle having the same area as the 2-D intercept of the spark at the time of peak amplitude and the plane located at half this amplitude (i.e., the *x*–*y* region where $\Delta F/F_0$ was less than half-amplitude). At every point in time during its evolution, the spark fluorescence is a function of *x* and *y* that resembles a bivariate Gaussian (examples in Fig. 1 A). An alternative set of parameters was derived by fitting to every spark in every image a bivariate Gaussian function. Parameters of fit included two coordinates of the center, an amplitude, and elliptic semi-axes (a and b). In this description, the FWHM is equal to the geometric mean ($(2a \times 2b)^{1/2}$) of the two elliptic axes. Both definitions of parameters yielded essentially identical results.

Other numerical routines were used to produce subsets of the 4-D database, including 3-D (*x*-*y*-*t*) series at constant *z* and 2-D (*x*–*t*) series at constant *z* and *y*. In turn, these simpler subsets were analyzed for event detection and flux calculation by programs

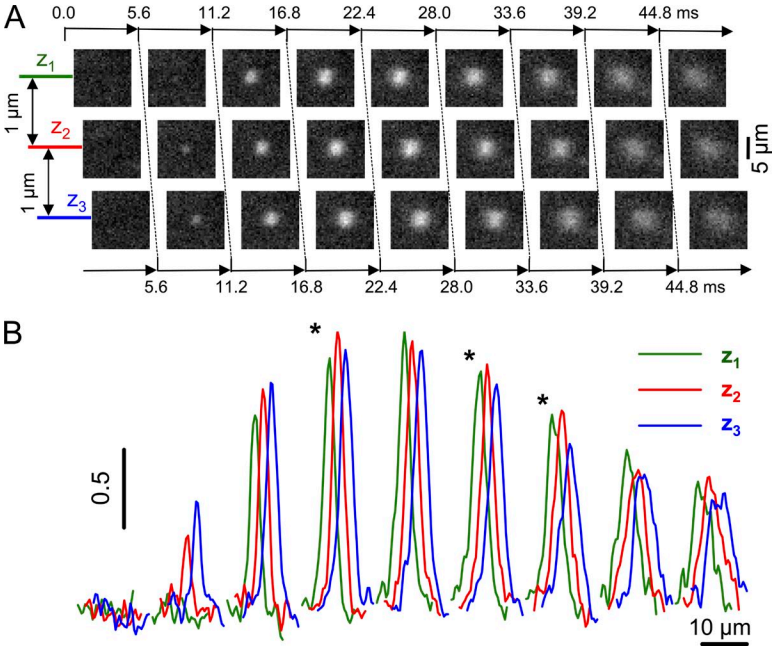

Figure 1. Scanning in three dimensions of space and time. (A) Square sections of successive *x*–*y* scan images of fluorescence of an atrial cardiomyocyte. As illustrated in the diagram, the vertical positions correspond to the *z* positions of three scanned planes ($z_1 = -1$ µm, $z_2 = 0$ µm, and $z_3 = +1$ µm). As indicated by the horizontal arrows, the acquisition time for a trio of *x*–*y* scans was 5.6 ms. (B) Profiles ($\Delta F(x)/F_0(x)$) at the central y value of the images in A, color-coded to *z* value. Asterisks mark image trios where the amplitude was largest in z_2. The example spark appears to be in focus.

developed earlier (Cheng et al., 1999; Brum et al., 2000). All of the numerics were implemented in the IDL programming environment (ITT Visual Information Solutions).

Methods to decide whether a spark is in focus

A spark that appears to be in focus is illustrated in Fig. 1. In Fig. 1 B, fluorescence intensity profiles (2 pixels wide) of intensity traced through the centers of the sparks, of which all correspond to the same location in successive images (Fig. 1 A), are shown. It can be seen that in several trios of images, the peaks of fluorescence in the z_2 plane are greater (asterisks) than in the z_1 and z_3 planes. This spark therefore satisfies the simplest criterion for being in focus, namely, that its amplitude be greatest in the central plane, z_2. This simple criterion, however, failed for several reasons. It is strongly biased toward acceptance of sparks of narrow width and is susceptible to limitations in scanning speed, limitations that will become clearer when describing Fig. 5. After testing several other procedures, we opted for a "three-point criterion," so named because it uses asymmetrically all three measures of amplitude, from all three focal planes (z_1, z_2, and z_3). The criterion, which is described in the Appendix, allows defining the 2-D vertical thickness of the slice where the sparks must originate to be considered in focus. All sparks deemed to be in focus in this study were identified by this criterion, with $2D = 0.2$ μm.

Reconstruction of line-scan images from 3-D scans

One of the aims of this work is to compare the properties of sparks imaged in focus with those inferred from images obtained in line-scan mode, which include sparks that may or may not be in focus. For this purpose, we derived from the database of 4-D series a set of images equivalent to line scans. The extraction of such reconstructed line scans is illustrated with Fig. 4 A.

For each image at a single value of z ($z_2 = 0$ μm), a line was extracted, namely the group of 512 values $F(x_j, y_n, z_2)$ at a set value of y ($y_n = 6$ μm, the approximate center of the range of y values), with j varying from 1 to 512. The lines extracted at the same y and z values in 1,000 successive images constitute together a 2-D series $F(x_j, t_k)$, the reconstructed line-scan image (with k varying from 1 to 1,000). One such line scan is represented in Fig. 4 A. The interval between sets of *x-y-z* scans (or the interval between *x–y* trios) was 5.6 ms, which is then the temporal increment of the line scan.

RESULTS

Cat atrial myocytes, which are devoid of a t-tubular system (Hüser et al., 1996), are known to generate spontaneous Ca^{2+} sparks from RyR clusters located in the nonjunctional SR (nj-SR) membranes (Sheehan et al., 2006). Thus, atrial Ca^{2+} sparks from nj-SR result entirely from SR Ca^{2+} release and lack any potential component from Ca^{2+} influx. We studied Ca^{2+} spark properties in these cells using a fast slit confocal scanner (cf. Toomre and Pawley, 2006, for brief description) in combination with a fast piezoelectric focusing attachment to acquire confocal *x–y* images successively in three vertical planes, at 1-μm separation. The imaging process, which we call 4-D scanning, is illustrated in Fig. 1 (see Table 1 for a list of terms and symbol definitions). Fig. 1 A includes a series of images from an atrial cardiomyocyte (with plasma membrane permeabilized and in a solution containing fluo-4). Square regions from the successive images are shown, including a spark that appears to be in focus. The relative position in the figure of each square image in the horizontal direction suggests the time at which it was acquired, whereas the vertical positions in the figure correspond to the three z positions of the scanned planes ($z_1 = -1$ μm, $z_2 = 0$ μm, and $z_3 = +1$ μm). Fig. 1 B plots the central profiles $(\Delta F(x)/F_0(x)$, where x corresponds to the longitudinal axis of the cell) through every frame, color-coded to z position.

The example spark shown in Fig. 1 appears to be in focus because it is somewhat more intense in the central (z_2) plane of scanning (asterisks in B mark image trios where the amplitude was largest in z_2). As stated in Materials and methods, the simple criterion that an in-focus spark would be detected with greater amplitude in the central plane led to biased results. Therefore, the three-point criterion (cf. Appendix), which is also satisfied by this example, was used to identify in-focus sparks. In the following sections, we will explore the properties of sparks in focus and compare them with those of all detected sparks.

Properties of in-focus sparks

An algorithm of automatic detection developed for *x–y* images (Brum et al., 2000) was applied to 34,000 *x-y-z* scans (i.e., trios of *x–y* images at three *z* values) obtained from 34 cells at 1,000 *x-y-z* (or 3,000 *x–y*) scans per cell. In these, 6,906 sparks were detected, of which 767 were found to be in focus by the three-point criterion.

The histograms of amplitudes (defined as a = peak $\Delta F/F_0$) of the two groups are represented in Fig. 2 A. Note that the histogram of all sparks detected (Fig. 2 A,

TABLE 1

List of symbols

Symbol	Description
$x, y, z,$	Spatial coordinates (x, horizontal, axial; y, transverse; z, vertical)
r, φ	Polar spatial coordinates (radial and angle)
$F, F_0, F/F_0, \Delta F/F_0$	Fluorescence, initial, normalized, increase
a, FWHM, T	Spark amplitude, FWHM, rise time
$g(a), l(a), u(a)$	Probability density of the distributions of amplitude (in focus, 3-D, 2-D)
$G(a), L(a), U(a)$	Histograms, sampling of the distributions $g(a)$, $l(a)$, $u(a)$
$h(z,\sigma)$	Gaussian function of vertical coordinate z with standard error σ
ζ	Vertical separation of spark source and focal plane
δ	Normalized difference in fluorescence (defined by Eq. 1)
$C3$	"Three-point criterion" (limit value of δ for sparks in focus)
D	Half depth of slice in focus, μm
ρ	Pearson's linear correlation coefficient
$[Ca^{2+}]$, $[Ca^{2+}]_{cyto}$, $[Ca^{2+}]_{SR}$	Free Ca^{2+} concentration, in cytosol, in SR
N, P_o, i	Number of channels, channel open probability, unitary current

dashed black line), referred to as $L(a)$, is monotonically decreasing, except for a region of the domain at low values of a (<0.4), where detection fails. In contrast, the histogram of in-focus spark amplitudes (Fig. 2 A, $G(a)$, solid green trace) features a mode at about $a = 0.7$. The implications of the distribution of amplitudes of sparks in focus will be fully considered in Discussion.

In Fig. 2 B, we compared in the same way as in Fig. 2 A the spatial width (FWHM) of detected sparks. In this case, the differences between the values reported for in-focus sparks and those of all detected sparks were much smaller; both distributions spread asymmetrically around a mode, close to 2.6 µm, but the distribution of in-focus sparks was slightly narrower. Clearly, the measurement of spatial width is much less compromised by out-of-focus error than that of spark amplitude.

In Fig. 2 C, histograms of rise time T (from the time of first detection to that of peak amplitude) are shown. T was measured always in the central plane (z_2). This resulted in a temporal resolution of 5.6 ms per image and consequently a coarse distribution. It is also necessary to point out that rise time here is defined as starting from the frame of first detection. This definition underestimates the true rise time and will warrant a reinterpretation of measured times (compare below).

These cells produced on average rather wide sparks of moderate amplitude. Averages of these parameters are listed in Table 2 for the 4-D, 3-D, and 2-D datasets.

The newly found method to identify sparks in focus obviously allows for a variety of other studies. Wang et al. (2004) found a quantized distribution of the rates of rise of fluorescence, indicative of quantized levels of flux, in sparks of peripheral couplons located in focus by activation of ventricular myocytes via loose patch clamp. To compare, and even though the present imaging was done at a much coarser temporal and spatial resolution, we computed initial rates of rise of fluorescence (rate of rise in a 5.6-ms interval from first detection) for individual sparks in the in-focus group. The values had a broad distribution between 0.01 and 0.12 ms^{-1}. There was no evidence of quantization.

Morphometric parameters of in-focus sparks are weakly correlated

In addition to the morphometric parameter values, other properties of sparks with interesting mechanistic implications are the correlations among these parameters. The correlations found in published studies have been poor for sparks of both skeletal and cardiac muscle cells. For example, linear correlation coefficients (Pearson's ρ) between rise time and amplitude of 0.09 and 0.12 were found in two studies of frog skeletal muscle (Ríos et al., 1999, 2008). In cardiac myocytes, correlations between amplitude, rise time, and width revealed ρ values between 0.07 and 0.17 (Shen et al., 2004).

A chief factor determining the poor correlations is the contribution to the variance in amplitude by the out-of-focus error (i.e., the absence of knowledge of the separation ζ between scanned line and spark source), which amounts to between 80 and 90% of the total variance (Ríos et al., 2008). The newly found ability to identify sparks in focus should remove the uncertainty of location, therefore reducing the out-of-focus contribution

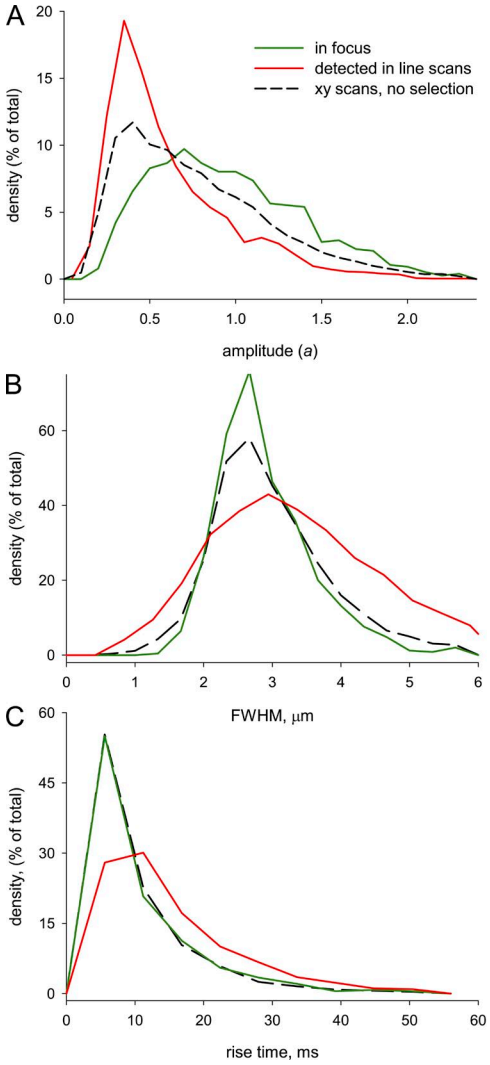

Figure 2. Properties of sparks in focus. Histograms of amplitudes (A), FWHM (B), and rise time (C) for all sparks detected in *x*–*y* scans (black, dashed), sparks in focus (green), and sparks detected in reconstructed line scans (red). Note that the amplitude histograms differ greatly among the three groups of sparks, but the other distributions diverge less. In-focus sparks have greater amplitudes and a mode in the distribution of this variable. Their modal width is not very different than that of the other groups, and their rise times are nearly identical to those of the entire set of detected sparks. The distribution of amplitudes measured in reconstructed line scans is heavily biased toward low values, whereas those of widths and rise times are more disperse than the corresponding ones in *x*–*y* scans. Relevant parameters of these distributions are listed in Table 2.

TABLE 2

Average morphometric parameters of sparks in various dimensions

Mode	Amplitude	Rise time	FWHM	N sparks
		ms	*μm*	
4-D	1.05	13.5	3.35	767
In-focus	(0.01)	(0.24)	(0.02)	
3-D	0.82	10.7	3.18	6,906
	(0.005)	(0.10)	(0.01)	
2-D	0.61	17.4	3.85	2,910
	(0.007)	(0.22)	(0.03)	

The SEM is in parentheses. The row with heading "4-D In focus" lists values for sparks detected in *x-y-z-t* series, the 4-D mode, which satisfy the in-focus criterion. *x-y-z-t* series were obtained from 34 cells; each series consists of 1,000 trios of *x–y* images successively at three *z* positions, for a total of 3,000 images per series. The row with heading "3-D" includes all sparks detected in *x-y-t* series at the z_2 position ($z = 0$), whether or not they were in focus. "2-D" refers to sparks detected in line-scan images constructed from the *x-y-t* series at position z_2 as described in Materials and methods. Fig. 4 has an example line-scan image constructed this way. It should be noted that the three modes (4-D, 3-D, and 2-D) are just different ways to analyze the full 4-D database.

to the variance in amplitude, and thus provide a better gauge of existing correlations.

The correlations among the parameters amplitude, rise time, and FWHM are illustrated by joint histograms in Fig. 3. The left-side panels represent the histograms of all sparks (3-D mode), whereas the corresponding histograms of events in focus are on the right side. Positive correlations were found in every case and were usually modest. Amplitude and width had ρ = 0.04 for all sparks and 0.14 for those in focus. For rise time and width, ρ increased from 0.14 to 0.26 in going from all sparks to those in focus, whereas for rise time and amplitude, ρ increased from 0.33 to 0.36. In sum, correlations between all three morphometric parameters were

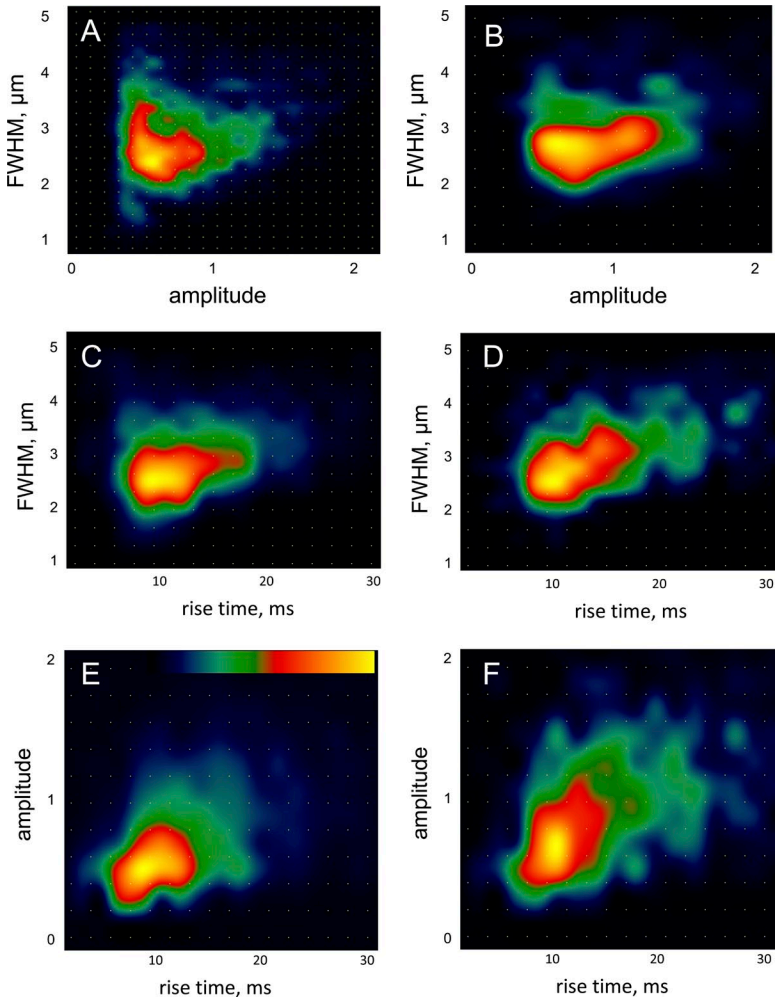

Figure 3. Correlations between spark parameters. Joint histograms of amplitude and width (A and B), rise time and width (C and D), and rise time and amplitude (E and F) for the set of all sparks detected in *x–y* images (A, C, and E) and for in-focus sparks (B, D, and F). The total number of sparks included was 6,906 (all sparks) and 767 (in-focus sparks). The first-order correlation coefficient ρ (*a*, FWHM) was 0.037 for all sparks and 0.14 for sparks in focus. ρ (*T*, FWHM) was 0.14 (all) and 0.26 (in focus). ρ (*T*, *a*) was 0.33 (all) and 0.36 (in focus). The color table starts at 0 (black) for all panels, whereas the maximum (yellow) corresponds to 143, 35, 201, 85, 149, and 70 events, respectively, for A–F.

positive and modest, and all of them increased for sparks in focus. The strongest positive correlation was found between rise time and amplitude. The issue of correlations will be encountered again when considering properties of averages of sparks.

The most relevant advantage of identifying sparks in focus is that the local Ca^{2+} transient, determined with minimal error, can then be used to derive the underlying flux of Ca^{2+} release. This will be done in the Discussion section.

The morphometric properties of sparks in line-scan images

It seemed interesting to compare the presumably true properties of sparks revealed by the present technique with those found using the line-scan (or 2-D) mode, which is still the standard of spark acquisition. A set of images equivalent to line scans was derived from the database of *x-y-z-t* series as described in Materials and methods and analyzed to derive their morphometric parameters in the standard way. One reconstructed line scan is shown in Fig. 4 A. A total of 2,910 sparks in 2-D were derived from the 4-D database. The number is less than in the *x-y-t* or 3-D case (6,906) because the method used one line per *x–y* image at a fixed *z* value and therefore missed a substantial portion of the images, resulting in fewer identified sparks. From these numbers, and considering that the length of scanning inside cells was on average 117 µm, a frequency of events can be calculated as $f = 2{,}910 \times (117\ \mu m)^{-1} \times (5.6\ s)^{-1} \times (34\ cells)^{-1} \times 100 = 13.1\ events \times s^{-1} \times (100\ \mu m)^{-1}$.

The histograms of amplitude, rise time, and spatial width of this group are represented in red traces in Fig. 2. The histogram of amplitude (referred to as $U(a)$) decays monotonically (except in a region of low amplitude, $a < 0.4$, where density increases as a result of increased detectability) and with positive curvature, in agreement with expectations from the theory of line-scan imaging (Ríos et al., 2001, and Discussion). The histogram of FWHM is broader for the 2-D case (Fig. 2 B, red), but other properties (like mode and skewness) are robustly conserved in all dimensional approaches (i.e., 2-, 3-, and 4-D). A similar broadening occurs with the histogram of rise times (Fig. 2 C).

DISCUSSION

This work evaluates quantitatively the properties of sparks imaged in focus, based on the availability of a fast confocal scanner, which combined with a rapid change-of-focus mechanism allows for actual scanning in three spatial dimensions. This mode of scanning can be repeated at a rate sufficient to characterize the evolution of sparks in space and time.

4-D scanning can be used to define sparks in focus

The identification of in-focus sparks reliably and reproducibly hinges critically on a robust criterion for the identification of the optical plane from where the sparks originate. Several approaches have been proposed. Sparks elicited by sparklets, the highly localized Ca^{2+} signal originating from Ca^{2+} entry through voltage-gated Ca^{2+} channels in the cell membrane near a patch electrode, are considered to be in focus (Wang et al., 2001, 2004), whereas the simultaneous recording of cytosolic sparks and the corresponding intra-SR Ca^{2+} depletion signal (termed Ca^{2+} blinks; Brochet et al., 2005) is an objective

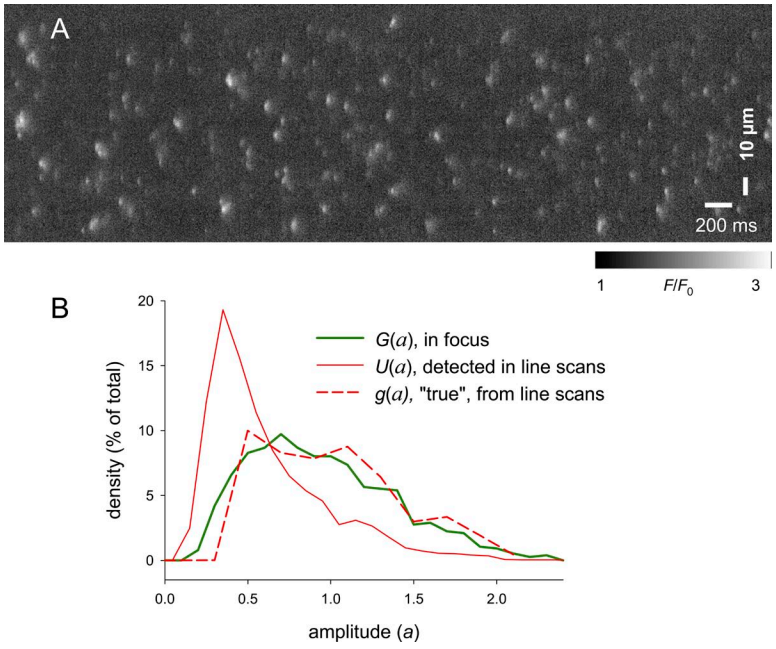

Figure 4. Properties of in-focus sparks derived from line-scan images. (A) Line-scan image reconstructed from 1,000 trios of *x–y* images obtained successively, at 5.6-ms intervals, from the same cell. The image is formed by one line of pixels taken from the central (z_2) image of every trio, at 512 values of *x* and one value of *y* ($y = 6$ µm). Size of image was reduced (from 512 × 1,000 to 298 × 1,000) by eliminating pixels corresponding to *x* values outside the cell boundary. Lines are placed vertically in the figure and stacked from left to right. One reconstructed line scan was derived for each of 34 cells studied. (B) Red solid trace, $U(a)$: histogram of amplitudes of 2,910 sparks detected by the conventional algorithm from all 34 reconstructed line scans. This plot is also in Fig. 2 A. Dashed trace, $g(a)$: distribution of "true" amplitudes derived substituting $U(a)$ for $u(a)$ in Eq. 1. Green trace, $G(a)$: amplitude histogram of sparks in focus, reproduced from Fig. 2 A.

criterion that circumscribes the location to the smaller volume where the blink signal can be detected (Zima et al., 2008a,b, 2010). Here, we demonstrate a novel approach, which relies on the near-simultaneous imaging of Ca^{2+} sparks in multiple planes and a robust criterion to determine where the spark originates.

In principle, a straightforward criterion for deciding whether sparks are in focus would be a fluorescence signal greatest in the central (z_2) plane. This criterion was not useful for several reasons. It was biased toward the detection of narrow sparks, and it did not take into consideration the fact that spark amplitude changes during the time it takes to acquire one *x*-*y*-*z* stack. Another limitation is that the criterion, consisting in simply comparing pairwise the amplitudes at z_2 and the other two planes, does not use all the information available. An alternative approach was based on the realization that separation from the focal plane, in either direction, resulted in asymmetric and predictable changes in the measurements at z_1, z_2, and z_3. In other words, if the center of a spark moves away from the central plane, the measured amplitude at the central plane decreases, but the other two measures, at z_1 and z_3, change in opposite directions. These simple considerations, together with the fact that sparks are extremely well described by Gaussian functions of space, were combined in the three-point criterion (Fig. A1 in Appendix). The criterion had the additional advantage of an adjustable stringency associated with a measure of the depth of the volume where events would be identified as being in focus.

In principle, it is not possible to know whether or not a selection process works correctly. This is simply because there is no known comparable population of in-focus sparks. We used instead two properties expected of a good selection. One is that the quantitative properties of the group of sparks classified as in focus should converge as the criterion is applied with increasing stringency (Appendix, Fig. A2). Additionally, the limiting properties to which sparks converge should be consistent with predictions made by the theory of line scanning (Shirokova and Ríos, 1997; Izu et al., 1998; Cheng et al., 1999; Ríos et al., 2001). Reliance on this theory seems justified, as some of its predictions have been quantitatively confirmed with simulations (Ríos et al., 2008), whereas others are consistent with sparks observed under special conditions, which assure their being in focus (Bridge et al., 1999; Soeller and Cannell, 2002, 2004; Wang et al., 2002, 2004).

As illustrated in Fig. A2, we found convergence of the histogram of amplitudes as stringency increased (within the limitations of the test). Specifically, the distribution of amplitudes lost density at low amplitudes and increased it at higher amplitudes, as predicted by the theory. There were no major changes in rise time and spatial width, other than a slight narrowing of the distribution of spatial widths, again consistent with expectations for sparks in focus. In increasingly stringent applications of the selection procedure, we also found convergence of width and rise time. In the next subsection, we evaluate quantitatively the agreement between observations and predictions by the theory of line scanning.

In-focus sparks have a preferred amplitude

A meaningful characteristic of sparks imaged in focus is a histogram of amplitudes $G(a)$ with a modal value (Fig. 2 A). This is in sharp contrast with the distribution of amplitudes reported by line or 2-D scanning. First, note here the distinction between $U(a)$, the histogram of amplitudes reported by line scanning, and $u(a)$, the distribution that such a histogram samples. $U(a)$ could be found in the present work, for the same group of images, as the histogram of amplitudes of the sparks found by applying our automatic detector to line scans reconstructed from sequences of *x*–*y* frames at z_2. The reconstructed line-scan images are illustrated in Fig. 4 A, and the $U(a)$ of such line scans is in Fig. 2 A (red trace). According to the theory of line scanning, $u(a)$ is a monotonically decaying function. $U(a)$ is consistent with the expectation, except for a rise explained by missed events at very low values of *a*.

Ríos et al. (2001) provide an equation,

$$g(a) = -\frac{1}{2\pi\sigma^2}\frac{d\left(a \cdot u(a)\right)}{da}, \tag{1}$$

to derive the distribution of true spark amplitudes $g(a)$ from $u(a)$. In Fig. 4 B, we reproduce $U(a)$ from Fig. 2 A (red, solid), and plot (red, dashed) the estimate of $g(a)$ obtained substituting $U(a)$ in Eq. 1. This estimated $g(a)$ compares reasonably well with $G(a)$, reproduced from Fig. 2 A (green). The agreement serves both as additional confirmation of the new method to define sparks in focus and as confirmation of significant properties of Ca^{2+} sparks.

Specifically, we confirm earlier conclusions, reached for both skeletal and cardiac ventricular muscle, that sparks have a preferential amplitude. In both tissues, the conclusions applied to special conditions. In the case of skeletal muscle, a modal amplitude was found in $g(a)$ functions derived via Eq. 1 in cells exposed to low concentrations of caffeine (Ríos et al., 2001). In cardiac muscle, a modal $G(a)$ was found in sparks elicited by sparklets near a patch electrode (therefore considered to be in focus; Wang et al., 2001, 2004). A modal amplitude was also found for groups of sparks originating from the same location in a cell, presumably from a single couplon firing repetitively (Bridge et al., 1999; Soeller and Cannell, 2002). Furthermore, the amplitudes of local SR Ca^{2+} depletion signals corresponding to Ca^{2+} sparks (Ca^{2+} blinks) reveal a modal distribution (Zima et al., 2008b).

As stated in earlier work, the main implication of the existence of a preferential amplitude of sparks is that

their sources are not single Markovian channels (Bridge et al., 1999; Ríos et al., 2001; Wang et al., 2001, 2004). The existence of a mode in the distribution of amplitudes has been reproduced by models in which sparks are generated by channel clusters, interacting via CICR, calcium-dependent inactivation, or mechanical contact.

Although the simplicity of the procedure to find sparks in focus and its initial tests and results are reassuring, there are also inherent limitations to the method. First, only three vertical (z) positions were scanned, and the spatial resolution was set low in every dimension (as a compromise between the increased volume of data and the finite rate of data acquisition). Second, the vertical scanning reduced the time resolution of the recordings (in our case to 5.6 ms between successive *x-y-z* scans or image trios), which particularly affects the accuracy of the recording of rapidly changing features of the fluorescence signal, such as the rise time.

The properties of sparks in focus can be determined with precision

Fig. 5 shows averages of 150 sparks that were found to be in focus and had the additional common property of a $T = 11.2$ ms. What this means is that the peak amplitude was reached two frames later than the frame of first detection. This number, 11.2 ms, has precision limited by the large (5.6-ms) interval. In Fig. 5, images are arranged in three columns and nine rows. Each column contains averages at the same z position. Each row represents images (image trio, cf. Materials and methods) obtained in the same 5.6-ms interval. The interval of first detection is labeled c. At this time, the spark became sufficiently different from noise to be accounted for by the detection algorithm. The time of first detection ($t = 0$) occurs substantially later than the start of the event. This is clearly shown in Fig. 5, where the sparks that form the average started to develop in row a, while they were first detected 11.2 ms later in row c. The discrepancy between start of the event and time of detection is the result of the chosen stringency of the spark detection algorithm, and leads to an underestimate of rise time (by ~11.2 ms).

It should be kept in mind that the images were obtained in the order z_1, z_2, z_3. This means that images on the right-most column were obtained later, resulting in a systematic excess in amplitude during the rising phase and a corresponding deficit during the decaying phase. These differences are especially noticeable at times when the spark is changing rapidly (as in rows b, c, f, and g). At these times, the simple expectation that an in-focus spark should be measured with greatest amplitude at z_2 is clearly invalid. This property helps explain why a more elaborate criterion was needed to decide whether a spark is in focus.

The morphometric parameter values of this average are fairly representative of the histograms in Fig. 3. The amplitude is 1.04, and the FWHM is 2.98 μm. The averaged spark data (Fig. 5) were also used for the Ca^{2+} release flux calculation discussed in the next subsection.

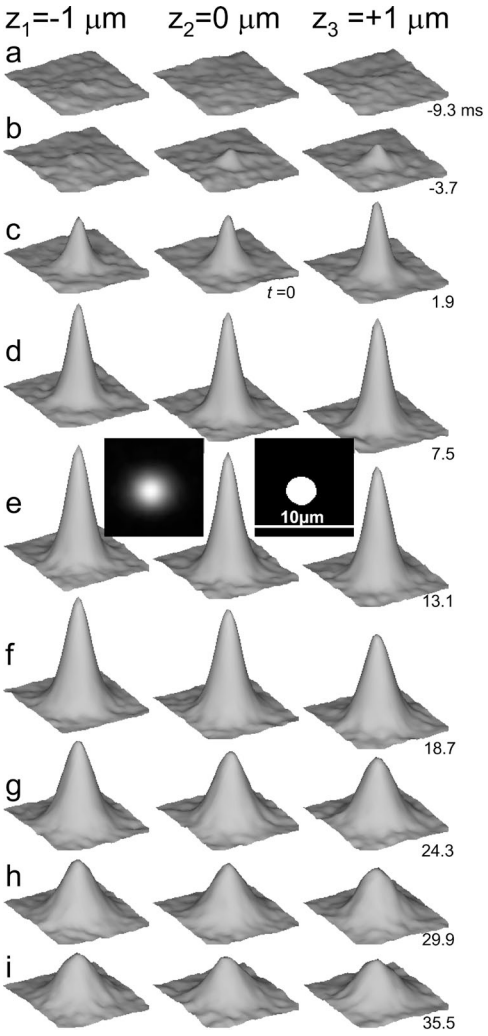

Figure 5. The average spark of $T = 11.2$ ms. Averages of images, at different times and z positions, of 150 in-focus sparks with $T = 11.2$ ms. Each column of nine panels contains successive averages at the vertical (z) position listed at top. Each row has the average images obtained at vertical positions z_1, z_2, and z_3 in the same 5.6-ms interval. The interval of first detection is labeled c. The times of acquisition of the images at level z_3 are listed in the third column. The origin of time ($t = 0$) is that of first detection, which occurs substantially later than the start of the event. Note that the spark average at z_2 has greater fluorescence than those at z_1 and z_3 only for the trio obtained at the time of peak amplitude, row e. During the stage of rapid rise of fluorescence, the averages at z_3 are greatest, whereas during the declining phase, it is position z_1 that records the greatest waveforms. The left-side square panel in row e depicts the average spark at the time of peak amplitude, at z_2, in grayscale. The right-side square panel shows in white the x–y region where average F/F_0 is greater than its half-maximum value.

Flux of Ca^{2+} release can be reliably estimated

A key advantage of knowing that a spark is in focus is that the underlying flux of Ca^{2+} release can then be derived with greater confidence. We calculated release flux applying the "backwards" method (Ríos et al., 1999) to averages of in-focus sparks of the same rise time (in the example of Fig. 5, $T = 11.2$ ms). The calculation, as implemented in Ríos et al. (1999) assumes radial symmetry for the event. The assumption applies well to the present case. This is demonstrated graphically for the average at $T = 11.2$ ms by the black insets in row e of Fig. 5, which show the average at its peak in grayscale (left) and a mask (right) formed by the contour of the average in the region where its fluorescence is greater than half amplitude. This contour is an almost perfect circle, a symmetry that applies to the average but does not preclude asymmetries in the individual sources. Furthermore, as detailed in Materials and methods, two measures of spatial width, in orthogonal directions (x and y dimension), were obtained for every spark, and this was done both by measuring diameters at half-maximal amplitude and by fitting a bivariate Gaussian to the spark. We found no significant difference between the average values of the two orthogonal measures, which is of course expected if the average is symmetric.

The method of release flux calculation requires assigning values to concentrations and kinetic parameters of the relevant Ca^{2+}-buffering molecules and removal systems, which was done as in our earlier work (Santiago et al., 2010). The Ca^{2+} buffers and removal processes included in the calculation are listed, with their parameter values, in Table 3. The use of permeabilized cells is advantageous for flux calculations because the cytosolic composition is precisely known. The calculation did not attempt to correct sparks for the blurring effect of the imaging process; the effects of blurring and the deblurring correction on calculated flux were found to be minor by Ríos et al. (1999), especially in cases where the sparks are spatially much wider than the point-spread function of the imaging system.

The calculation and results are illustrated in Fig. 6. In Fig. 6 A is the fluorescence, averaged over the angle φ (as shown schematically in inset a), plotted as a function of radial distance r and time from first detection. Inset b shows the same fluorescence in pseudocolor. That the fluorescence is averaged first over 150 events and then over the polar angle explains the near absence of noise in the result.

The calculated release flux is in Fig. 6 B. The spatial size of the source, which can be appreciated in inset c, is very small compared with the fluorescence event.

Quantitative aspects of the flux are illustrated in Fig. 7. The radial profiles of spark and calculated flux are compared in Fig. 7 A. It can be seen that the flux largely originates at a region of ∼0.5 µm in diameter, which is roughly the spatial resolution of the microscope (a result suggesting that the source has dimensions below the limit of resolution). Fig. 7 B depicts temporal dependence of fluorescence (F/F_0), calculated free Ca^{2+} concentration (µM), and Ca^{2+} release flux (mM/s) for the same spark average. The peak Ca^{2+} release flux was calculated as 53 mM/s. Even though temporal aspects are not well described at this time resolution, it can be seen that the peak of the flux precedes the peak of free $[Ca^{2+}]$, and both precede the peak of fluorescence. The graph includes a plot of Ca^{2+} release current, calculated by integrating flux over the volume of the source. The current is approximately cotemporal with the flux and peaks at ∼11 pA. This value of peak current is at the higher end of the range of estimates in cardiac cells (Blatter et al., 1997; Izu et al., 2001; Cheng and Wang, 2002; Soeller and Cannell, 2002; Wang et al., 2004; Santiago et al., 2010). Such level of current would require 20–30 channels simultaneously passing currents of 0.3–0.5 pA (Kettlun et al., 2003). Although large, this number of channels is still consistent with a source that remains below the limit

TABLE 3

Release flux calculation

Binding site	Concentration	k_{ON}	k_{OFF}	Diffusion coefficient	Flux
	µM	*(µM ms)$^{-1}$*	*ms^{-1}*	*µm^2 ms^{-1}*	*mM/s*
ATP	5,000	Ca, 0.15	30	0.14	25.3
		Mg, 2e-3	0.2		
EGTA	350	4e-3	2e-3	0.07	0.6
Fluo-4	40	0.032	0.032	0.05	1.4
SERCA	47	0.5	0.5	N.A.	0.9
Troponin	70	5.7e-3	0.011	N.A.	0.1
Sarcolemma	42	0.1	1.3	N.A.	0.1
Free Ca^{2+}*	variable	N.A.	N.A.	0.35	24.7

Model parameters (concentration, reaction rates, and diffusion coefficients) are given for all Ca^{2+} ligands used in the calculation. The last column lists maximal contributions to the flux total by the binding of Ca^{2+} to the corresponding ligand. The last row lists the free Ca^{2+} term in the flux calculation (namely, the flux required to account for the local rate of change of $[Ca^{2+}]$ and diffusion of the free ion). With minor changes, parameters are as in Santiago et al. (2010) and references therein.

of optical resolution. It is also consistent with estimates of the number of contributing channels obtained by noise analysis of spark amplitudes (Bridge et al., 1999), as well as the number of RyRs per couplon derived from RyR binding (Hayashi et al., 2009) and immunostaining studies (Soeller et al., 2007; Cannell and Kong, 2012). The number of channels estimated here is much greater than that derived from the observation of quantized flux in sparks from peripheral couplons ($n < 6$; Wang et al., 2004). Cannell and Kong (2012) argue that a complex, multi-couplon source could reconcile the observation of quantal sparks with the greater estimates of channel numbers derived in other works and confirmed here.

The large number of simultaneously active channels in the present study is indicative of a greater than usual tendency of these channels to open. This tendency is manifested in the frequency of sparks detected in the reconstructed line scans (13.1 events; 100 μm^{-1} s^{-1}), which is greater than that reported in studies of intact atrial and ventricular muscle (ranging from ~0.5 to 5 events; 100 μm^{-1} s^{-1}: McCall et al., 1996; Satoh et al., 1997; Li et al., 2005; Sheehan et al., 2006; Copello et al., 2007; Santiago et al., 2010), but is only somewhat higher than frequencies observed in permeabilized ventricular cells (3–11 events; 100 μm^{-1} s^{-1}: Zima et al., 2003, 2004, 2008a,b, 2010; Qin et al., 2009). Part of the increase in frequency may therefore be attributed to an effect of membrane permeabilization, which has been demonstrated directly for the same cell type (cat atrial myocytes; Sheehan et al., 2006), and part to an actual difference between atrial and ventricular cells (cf. discussion below).

The calculation of flux permits an evaluation of the role of different buffer systems in shaping sparks. The calculation of Ca^{2+} release flux produces an estimate of the removal flux associated with every process that is

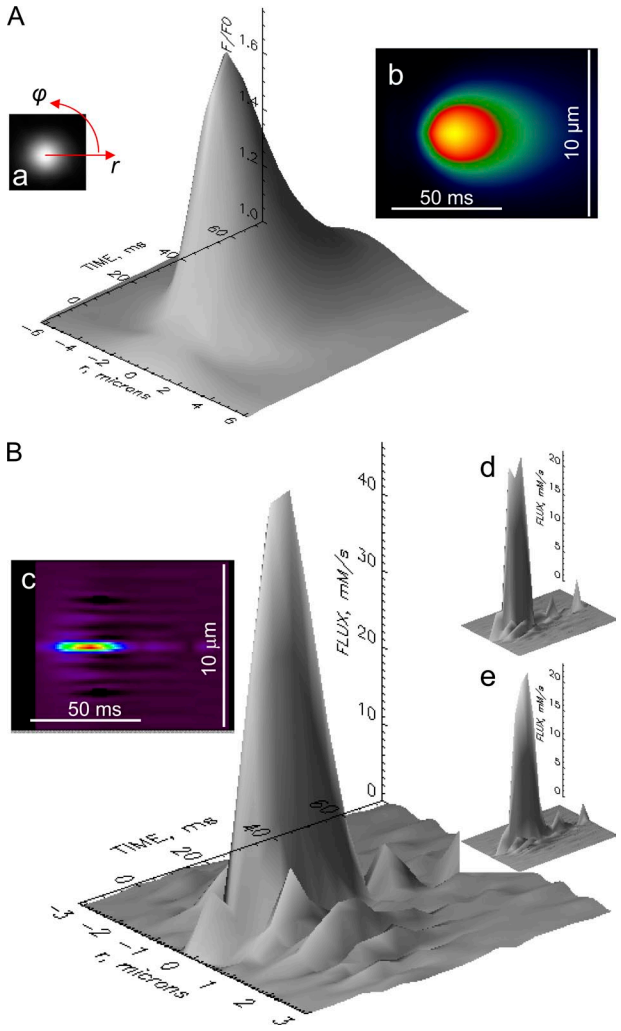

Figure 6. Ca^{2+} release flux of an averaged spark. (A) Normalized fluorescence, $F/F_0(r, t)$, obtained by averaging over the polar angle φ (as shown in inset a) the averaged spark of $T = 11.2$ ms (illustrated in Fig. 5). $F/F_0(r, t)$ is represented in pseudocolor in inset b. (B) Release flux, calculated from $F/F_0(r, t)$, represented as surface plot or in pseudocolor (inset c). The "ATP component" (specifically, flux of Ca^{2+} removal into ATP) and "free Ca^{2+} component" (flux needed to account for local rate of change of free $[Ca^{2+}]$ and diffusion of the free ion) of flux are separately plotted in insets d and e, respectively. Collectively, they constitute >90% of the total at the time of peak release flux (details in Table 3).

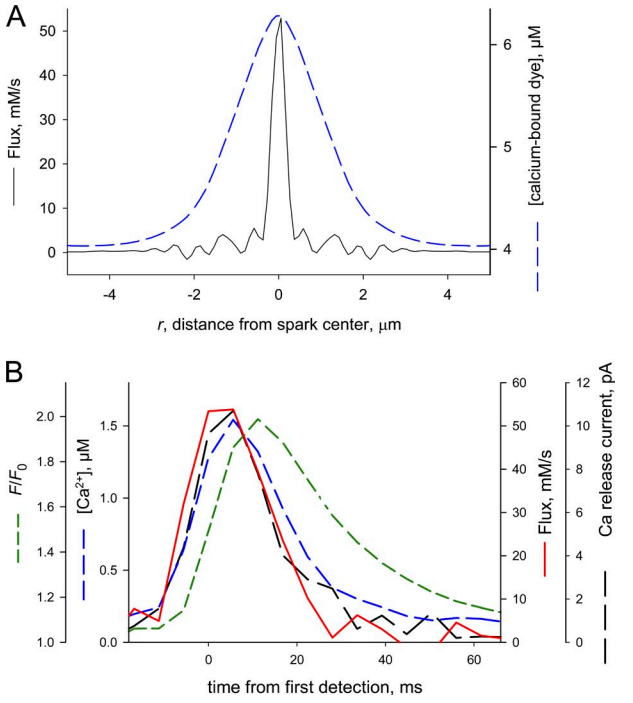

Figure 7. Quantitative properties of release flux. (A) Radial dependence of fluorescence (and its proportional magnitude, concentration of Ca^{2+}-bound fluo-4; dashed trace) at the time of its peak compared with that of calculated release flux for the average of sparks of $T = 11.2$ ms. Although the FWHM of the fluorescence spark was 2.98 μm, that of the flux was 0.45 μm. (B) Time course of spatial maxima of fluorescence (green), calculated free $[Ca^{2+}]$ (blue), release flux (red), and release current (black) measured in successive average images of sparks of $T = 11.2$ ms. Note that flux started to fall before the time of peak fluorescence, an occurrence common for sparks of $T \geq 11.2$ ms.

taken into account. The processes and their maximal calculated removal fluxes for the average spark at $T = 11.2$ ms are listed in Table 3. Of the six processes listed, ATP binding and free Ca^{2+} accumulation and diffusion contribute together >90% of the flux, and their contributions, plotted separately in insets d and e of Fig. 6, have approximately equal maxima.

In addition to stressing the importance of ATP in shaping fast cytosolic Ca^{2+} transients, a notion first introduced by Baylor and Hollingworth (1998), this observation implies that the assumptions regarding specific properties of other ligands are unlikely to affect the results in any significant way. In support of this inference, alternative calculations with threefold changes in either direction in the diffusion coefficients assumed for EGTA and dye caused negligible changes in the resulting flux. Naturally, changes in the assumptions for ATP and Ca^{2+} had a greater effect. The main conclusions, however, were upheld. For example, when the diffusion coefficient D_{ATP} was reduced (increased) by a factor of 2, peak release current decreased by 8% (increased by 12%). When D_{Ca} was reduced (increased) twofold, the peak current was reduced by 4% (increased by 8%). Kinetic milestones, however, including the time to peak flux, and whether or not flux decreased before the peak fluorescence, were not changed in any case.

Conversely, the concentration of free Mg^{2+}, which in turn defines the availability of ATP, becomes an important factor in shaping fast local Ca^{2+} transients.

Release flux and control of channel open time

The determination of spark properties and calculation of flux and current was done for spark averages differing by rise time T. Similar averages as illustrated in Fig. 5 were obtained by binning in-focus sparks according to T, between 5.6 and 28 ms (in increments of 5.6 ms). The five different values of T will be represented by T_j, with j varying from 1 to 5. The properties of averages of sparks of different T are illustrated in Fig. 8. Fig. 8 A plots the amplitudes at different times (with $t = 0$ defined as the time of first detection). A notable aspect is that the early stages of all these averages are fairly similar, with a stage of fast increase, of approximately equal rate for all averages, regardless of the time at which sparks reach peak amplitude. This common rate of rise indicates that the underlying flux of Ca^{2+} release is similar for the five groups (more implications of this observation are discussed below).

The spatial width of these averages is plotted in Fig. 8 B. As discussed above, spatial width, or FWHM, was well defined in the average spark data, independently of the direction in the x–y plane, and there was no significant difference between the average values of FWHM in two orthogonal directions (x and y dimension). This symmetry is inconsistent with the possibility that a spark is originated by an extensive source of size greater than the limit of resolution of the microscope. It is not inconsistent with an asymmetric source, constituted by multiple channels, provided that its size remains below the limit of spatial resolution.

Another intriguing property of these events is revealed by the study of widths. As the plots in Fig. 8 B show, there is no obvious difference in the evolution of width among sparks of different rise time, and the plots show no visible inflection at the times of the peaks. If there is no difference in width among the groups, it follows that release termination has no consequences for spark width. Models of spark production predict some increase in width associated with release termination, superimposed on the increase mandated by simple

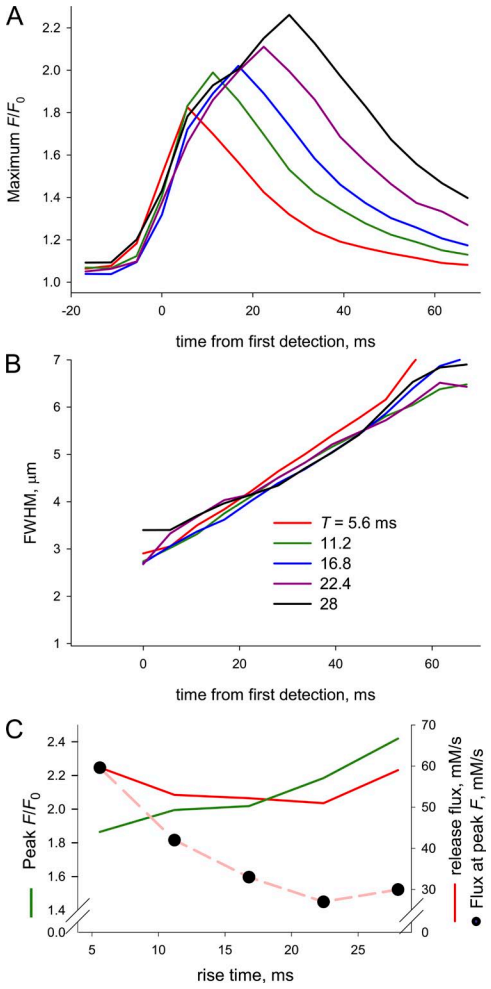

Figure 8. Properties of sparks of different rise times. (A) Amplitudes (i.e., maxima of F/F_0) at successive values of t (time from first detection) for averages of sparks of different T (coded as indicated in B). Note that the early course of fluorescence is similar for all averages (i.e., independent of T). (B) FWHM measured at different times on the same averages. The values are similar and evolve similarly with t for all averages. (C) Dependence of spark parameters with T. Peak fluorescence (green trace) grows with T. Peak flux (red) does not have a clear dependence on T. Flux at time of peak fluorescence (circles) decays monotonically as T increases.

diffusion (a phenomenon named "post-peak expansion" in Zhou et al., 2003). It can also be seen that the increase in width is essentially a linear function of time, in every case. Simple diffusion instead predicts an increase proportional to the square root of time. A possible reason for these discrepancies is that the theory in Zhou et al. (2003) assumes complete termination of Ca^{2+} release at the peak and a constant current during the postulated release time. As discussed below, neither condition is likely to be satisfied by the events observed here.

Peak fluorescence and flux in these averages of sparks of different rise time are summarized in Fig. 8 C. Note first that spark amplitude (i.e., normalized increase in fluorescence at the time of the peak, in green trace) increases with T. This property was already presented in Fig. 8 A. In its regard, we noted that the early, rapid rise in fluorescence was similar for all groups of sparks, regardless of their T, implying that release flux was similar, and maximal, for all averages at this early time. Peak flux, plotted in red, is indeed similar for all groups, and so is peak current (not depicted).

In Fig. 7 B (illustrating the group of sparks with a common T = 11.2 ms), it can be seen that the flux peaked at 5.6 ms, before the time of peak fluorescence. The peak of flux was reached at 5.6 ms in all other cases, implying that flux decayed during the rising phase of the spark. This is demonstrated in Fig. 8 C, where circles plot flux at the time of peak F for all five average sparks. That flux at the time of peak F is lowest for the sparks of longest rise time suggests that flux decreases monotonically during the rising phase.

These observations regarding the evolution of $[Ca^{2+}]_{cyto}$ and flux have important mechanistic implications. The main observations are as follows: (a) $F(t)$, hence $[Ca^{2+}]_{cyto}(t)$, dF/dt, and $Flux(t)$ are approximately the same for all groups, up until their respective peak times (T_j). (b) After an early maximum, which occurs at 5.6–11.2 ms, flux decays substantially during the rising phase of the sparks. Observation a suggests that $[Ca^{2+}]_{SR}(t)$ is also very similar for these groups, up until their respective peaks.

These data, plus observations in previous studies, provide constraints for interpreting the underlying channel behavior. Ca^{2+} release current is equal to $N{\times}Po{\times}i$, where $N{\times}Po$ represents the number of open channels in the couplon, and i represents the unitary channel current. Flux and current are proportional; therefore, a decreasing flux or current during the times T_j requires the decay of i, $N{\times}Po$, or both.

Previous works provide abundant evidence that i decays (because local depletion, inferred from simulations and demonstrated by blinks, implies a decrease in the Ca^{2+} gradient). $N{\times}Po$ is also expected to decay, as SR depletion has a well-established closing effect on channels (Sobie and Lederer, 2012). A satisfactory quantitative description of sparks and blinks in terms of the above factors, however, does not exist (the article by Sobie and Lederer, 2012, discusses the difficulties that any attempt at such description will find). The present observations, showing that sparks of very different rise times have essentially indistinguishable early stages, set additional constraints and challenges. At least in an approximate and average sense, it can be affirmed that both the number of open channels and the unitary current are evolving similarly (at times before T_j) in the sparks studied here. If that is the case, a justification for the different rise times is not evident. If rise times are associated with the time when most channels are open (as assumed in models of Shen et al., 2004, and Wang et al., 2004), the observation would imply that the open times are not controlled by $[Ca^{2+}]_{SR}$ as is widely believed, or that the control is exerted, but different groups of channels have different sensitivity to it. The latter interpretation is supported by indications that the $[Ca^{2+}]_{SR}$ level at which sparks terminate is variable among couplons, but is highly constant for a given individual release site (Zima et al., 2008a).

Other simulations suggest that the duration of the rising phase of sparks is determined by the interplay of depletion and the varying number of open channels (e.g., Sobie et al., 2002). Certainly, different rates of depletion, associated perhaps with different volumes of SR cisternae or different refilling rates (Picht et al., 2011), could result in fluorescence peaks at different times. The difficulty with such scheme is that it would predict a gradual divergence of F between the groups with different rates of depletion, rather than the sharp departure at T_j observed here.

In conclusion, the present observations add to the current picture of control the possibility of other, less deterministic mechanisms. One is closure of groups of channels triggered by depletion at very different $[Ca^{2+}]_{SR}$ levels. A second possibility is that control by $[Ca^{2+}]_{SR}$ is weakened and consequently sparks terminate for reasons other than local SR depletion (a conclusion consistent with the observation of long-lasting sparks of varied durations but constant $[Ca^{2+}]_{SR}$; Zima et al., 2008a). The latter could be a peculiarity of atrial cells, consistent with other indications that the feedback mechanisms that control Ca^{2+} release are weakened in these cells.

In-focus sparks have greater correlations between morphometric variables

As demonstrated by 2-D histograms in Fig. 3, the morphometric parameters a, FWHM, and T were positively but poorly correlated for sparks detected in 3-D (left-side panels). When the analysis was restricted to sparks in focus, the correlations increased in every case.

A positive correlation between rise time and amplitude is in contrast with previous observations. Indeed, in cardiac myocytes, Wang et al. (2004) noted a quantized distribution of rates of rise of fluorescence, which they

attributed to discrete numbers of participating channels (n_q) and a reduction of rise time for sparks of high n_q, which was interpreted as evidence that large currents reduced spark duration by closing channels. In cardiac myocytes, the correlation between amplitude, rise time, and width was weak (albeit positive; Shen et al., 2004). In skeletal muscle of amphibians, an absence of correlation between these variables was noted (Klein et al., 1999; Lacampagne et al., 2000). Ríos et al. (1999, 2008) found a small and not significant negative correlation, which upon a more refined analysis yielded significant correlation in two distinct regions: a region of low *T* where the correlation was positive, followed by one of significant negative correlation at longer *T*. Both an absence of correlation and a negative one require some sort of negative feedback that turns off channels when local cytosolic [Ca^{2+}] increases (or [Ca^{2+}] in SR lumen decreases). In the present case, however, a positive correlation was found. That it became more significant when the analysis was restricted to sparks in focus increases confidence in the finding. The positive correlation suggests that the negative feedback mechanisms on channel openness, implied by the aforementioned work, may be less important in atrial cells or under the conditions of the present experiments. The large flux and release current calculated for the observed sparks is also an indication of increased propensity of channels to open, as is the high frequency of these events.

The positive correlation observed between rise time and width is as predicted in spark models (for example, Jiang et al., 1999; Zhou et al., 2003). Finally, the positive correlation between amplitude and width (which follows mathematically when the other two correlations are positive) can be understood as the consequence of both variables increasing with increasing rise time (dependencies that were both found, as documented in Fig. 8). These simple positive correlations are predicted by models in which width and amplitude are determined largely by the duration of the underlying Ca^{2+} release current (which is positively correlated with rise time), rather than those in which longer durations of release are associated with smaller clusters of channels or lower unitary current. The latter associations are consequences of negative feedback mechanisms affecting channel openness. Therefore, these correlations are again indications of weakened negative feedback in the present case.

These cells were subjected to membrane permeabilization, which may have resulted in the increased spark size and frequency, in a way similar to the increase of spark size and frequency observed in cut versus intact skeletal muscle fibers (Baylor et al., 2002; Chandler et al., 2003) and in chemically permeabilized versus intact atrial myocytes (Sheehan et al., 2006), or the appearance of spark-like events in mammalian skeletal muscle cells when they are peeled or saponized (Kirsch et al., 2001).

On the other hand, this weakened negative feedback could be a feature of atrial myocytes, critical for Ca^{2+} release during excitation–contraction coupling (ecc). The lack of t-tubules in atrial myocytes requires a distinctly different mechanism of Ca^{2+} release during ecc. Although in ventricular myoctes all RyR clusters are found in close physical association with a dihydropyridine receptor (DHPR) Ca^{2+} channel in the surface membrane because of the extensive t-tubular system, in atrial myocytes only the RyRs of the junctional SR in the cell periphery are organized in a similar arrangement. Consequently, action potential–induced opening of DHPRs provides the required trigger Ca^{2+} for CICR simultaneously and homogeneously throughout an entire ventricular myocyte, but not in atrial cells. In atrial myocytes, DHPR opening triggers release initially only in the cell periphery, which leads to an elevation of subsarcolemmal cytosolic [Ca^{2+}] that initiates regenerative and propagating CICR from nj-SR. This centripetal propagation of CICR from nj-SR is reminiscent of cardiac Ca^{2+} wave propagation (Berlin, 1995; Hüser et al., 1996; Kockskämper et al., 2001; Mackenzie et al., 2001; Woo et al., 2002; Sheehan and Blatter, 2003). Ultrastructural studies (Kockskämper et al., 2001) showed that nj-SR membranes do not form the narrow diadic clefts that would allow [Ca^{2+}] to rise rapidly on the cytosolic face of the RyR. Thus, to achieve reliable and robust Ca^{2+} release throughout the entire atrial myocyte, other mechanisms need to be postulated. As demonstrated in the present study, the relative large Ca^{2+} flux underlying atrial sparks, the calculated large numbers of channels involved, the enhanced propensity of RyR channels to open, the extended spatial spread (see also Blatter et al., 1997), and a diminished influence of negative feedback mechanisms in this preparation compared with ventricular myocytes all contribute to a situation where lower [Ca^{2+}] levels are required to trigger CICR and propagation of activation during ecc.

Conclusions

We have demonstrated a method to image sparks that are in focus, based on scanning fluorescence in three spatial dimensions. The sparks found to be in focus had substantially greater amplitudes than the population of all detected sparks and, at variance with these, distributed with a broad mode (at $\sim 0.7\ F_0$). Properties of sparks in focus were determined both with accuracy, because the out-of-focus error was removed, and precision, given the large number of events recorded. Among the main morphometric parameters, amplitude was substantially different in the sparks in focus, whereas average width and rise time were not. The Ca^{2+} release flux and current underlying sparks in focus were large, requiring sources of 20–30 channels. The flux peaked early and then decayed during the rising phase of the spark, which is consistent with existing evidence of

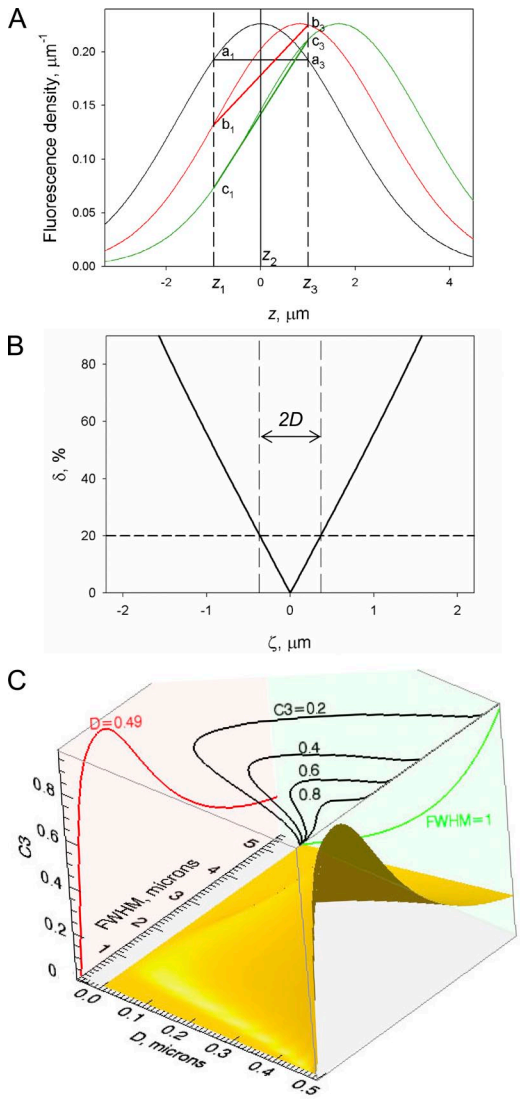

Figure A1. The three-point criterion for sparks in focus. (A) The spatial (z) profile of fluorescence of a spark, represented as a Gaussian function,

$$F = \frac{1}{\sigma\sqrt{2\pi}} e^{-\frac{(z-\zeta)^2}{2\sigma^2}},$$

of $\sigma = 1.4$ μm, centered at $\zeta = 0$ (black), 0.825 (red), or 1.65 (green). Segments a_1–a_3, b_1–b_3, and c_1–c_3 join the intersections of these curves with the lines at z_1 (−1 μm) and z_3 (+1 μm). The difference between the ordinates at these intersections increases as the central abscissa ζ moves away from $z = 0$. (B) δ, absolute value of the difference between fluorescence at $z = z_1$ and $z = z_3$, normalized by the value at $z = z_2$ (according to Eq. A1), and plotted versus ζ, the central position (z value) of the Gaussian spark. Note that sparks of $\sigma = 1.4$ μm will have $\delta < 0.2$ (or 20%) when their central z value satisfies the inequalities, $-0.37 \le \zeta \le 0.37$, in other words, when the origin of release is within a spatial slice of height 2×0.37 (or *2D*). (C) Generalization of the calculation in B to include σ as a variable. δ, calculated by Eq. A1, is plotted versus ζ and FWHM = $(2 \times \ln 2)^{1/2}\sigma$. This function works as a threshold criterion (hence it is labeled *C3*) as follows: given a set thickness *2D* of the slice of space deemed to be in focus, an experimentally recorded spark will be in focus if its calculated δ is ≤C3 at the set value of *D* and the FWHM measured for the individual spark. In the graph, the line plots are intersections of the *C3* (*D*, FWHM) surface by planes of constant *C3* (black), *D* (red), or FWHM (green).

significant local depletion of the SR, but could also be helped by progressive closure of channels in the cluster. The magnitude and evolution of flux were similar in sparks of different rise time. This feature indicates that the termination of Ca^{2+} release was not robustly controlled by variables associated with flux, including free cytosolic and free SR calcium concentrations, either because different channels responded to these variables in different ways, were controlled by variables other than $[Ca^{2+}]_{cyto}$ and $[Ca^{2+}]_{SR}$, or closed at random. The large sparks, large fluxes, and calculated large numbers of channels involved define a state of enhanced proclivity of channels to open, reflecting a diminished influence of negative feedback mechanisms in this preparation. The lack of association between flux and spark rise time can also be taken as an indication of a general deficit in negative controls, underlying the abundance of local events in these atrial cells. Because atrial myocytes lack a t-tubular system and have to rely on robust cell-wide propagating CICR for the activation of the contractile machinery, this deficit in negative control constitutes an advantage for ecc in these cells. Other properties of local events in focus, including spatial associations, event propagation, and location-specific aspects of Ca^{2+} release, can be studied advantageously with 4-D scanning.

APPENDIX

A robust procedure for identifying in-focus sparks

The purpose of this appendix is to describe and illustrate a procedure to decide, based on comparison of images at three values of the z coordinate, whether a spark is in focus. The procedure and associated criterion are called "three-point" because they use asymmetrically the measures of amplitude at the different z positions. In contrast, the simple criterion, whereby a spark is deemed in focus if its amplitude at z_2 is greater than at the other two z positions, uses the measures at z_1 and z_3 symmetrically, thus not taking advantage of all the information available.

The procedure is illustrated in Fig. A1. A spark is represented by a Gaussian function of the vertical coordinate z. The function has a standard error (σ) of 1.4 μm, which makes it representative of sparks in the present database. We will refer to this function as $h(z,1.4)$. Gaussian sparks with identical σ are depicted centered at two other positions on the z axis, separated by 0.825 μm—an arbitrary distance of convenience. Three vertical lines are traced at positions z_1 (−1 μm), z_2 (0 μm), and z_3 (+1 μm), representing the three planes of *x-y-z* scanning. The segments a_1-a_3, b_1-b_3, and c_1-c_3 are the intersections of the functions with the planes z_1 and z_3. Their vertical spans are therefore the differences between the spark intensity measured at the two extreme values of z. It can be seen that this difference, as a fraction of the central (z_2 = 0 μm) value, increases steeply as the spark moves away from the central plane.

The absolute value of the difference, as a fraction of the value at z_2, can be calculated as:

$$\delta \equiv \frac{h(-\xi-1,1.4)-h(-\zeta+1,1.4)}{h(-\zeta,1.4)}, \quad \text{(A1)}$$

where ζ is the separation between the focal plane and the center of the displaced spark. δ is represented as a function of ζ in Fig. A1 B. For absolute values of ζ <0.37 µm, δ is <0.2. In other words, when the difference between amplitudes at the two extreme z planes is <20% of the central amplitude, events of σ = 1.4 µm should be restricted to a slice 0.74-µm thick, centered by the focal plane at z = 0 µm.

Inspection of Eq. A1 and Fig. A1 shows that δ decays monotonically as ζ decreases, a property that was used to advantage to generate a scalable criterion for identifying in-focus sparks. Let δ, calculated by Eq. A1 for a set of values of ζ, be less than that calculated for a reference value of ζ, say, D. Because of the monotonic relationship, it follows that all ζ that satisfy the inequality δ (ζ) < δ (D) will be less than D. An equivalent statement is that the origins of sparks at such values of ζ will be contained within the slice of half thickness D. We represent δ (D), the "criterion" threshold, by the symbol *C3*. The criterion can be made applicable to sparks of other spatial widths simply by introducing the corresponding value of σ in place of 1.4 in Eq. A1. *C3* is therefore a function of D and σ (or the proportional quantity $(2 \times \ln 2)^{1/2}\sigma$ = FWHM). *C3* is represented as a function of D and FWHM in Fig. A1 C. (Note that *C3* grows monotonically with D, as shown by the projection in green, but has a modal dependence on FWHM, shown by the projection in red.) Indeed, for very narrow sparks, the δ value calculated by Eq. A1 is small because both terms in the numerator are small. For large values of FWHM, both terms become large but similar, so δ becomes small again.

This criterion proved to be superior for several reasons, which justify their use in the present work. One important advantage is that it satisfied expectations of convergence. Specifically, when this criterion was applied to the same universe of sparks at progressively narrower depths of the in-focus slice (set by the variable D), it produced groups of sparks tending to a limiting set of properties. This is illustrated in Fig. A2 with histograms of amplitudes of the groups of sparks selected by the three-point criterion at progressively lower values of D. As D decreases, the histograms converge to a distribution with greater density at high values of the amplitude. This analysis cannot be taken to a true limit as the spark numbers decrease with D, but the convergence seemed satisfactory as far as it could be explored. Moreover, the loss of density at low values of amplitude and gain at high values was as expected if the selection progressively eliminated out-of-focus sparks. Specifically, the histogram obtained with the criterion applied at a D of 0.1 µm (green trace in Fig. A2) appears to have limit features, while still including a large number of sparks.

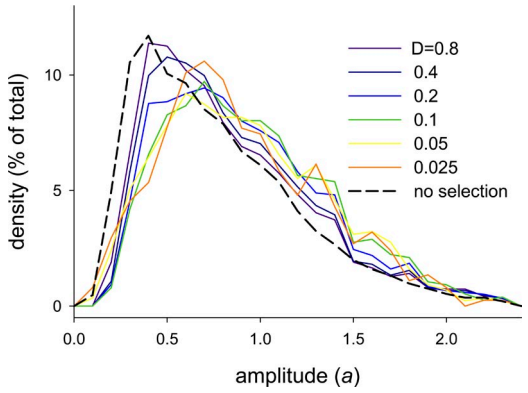

Figure A2. Convergence of the three-point criterion for identification of in-focus sparks. Histograms of amplitudes of sparks selected as in focus by the three-point criterion, at progressively lower values of D (half-depth of in-focus slice). Values of D are indicated on the graph. Note that the features of the histograms vary little at $D \leq 0.1$ µm. In this work, a spark was considered to be in focus if its δ, calculated by Eq. A1, fell below the *C3* value at the measured FWHM on the intercept of the C3 surface (Fig. A1 C) and the plane at D = 0.1 µm.

This work was supported by grants from the National Institutes of Health (AR049184, AR032808, and RR24707 to E. Ríos; HL62231, HL80101, and HL101235 to L.A. Blatter), and the Leducq Foundation (to L.A. Blatter).

Richard L. Moss served as editor.

Submitted: 23 August 2011
Accepted: 26 January 2012

REFERENCES

Baylor, S.M., and S. Hollingworth. 1998. Model of sarcomeric Ca^{2+} movements, including ATP Ca^{2+} binding and diffusion, during activation of frog skeletal muscle. *J. Gen. Physiol.* 112:297–316. http://dx.doi.org/10.1085/jgp.112.3.297

Baylor, S.M., W.K. Chandler, and M.W. Marshall. 1983. Sarcoplasmic reticulum calcium release in frog skeletal muscle fibres estimated from Arsenazo III calcium transients. *J. Physiol.* 344:625–666.

Baylor, S.M., S. Hollingworth, and W.K. Chandler. 2002. Comparison of simulated and measured calcium sparks in intact skeletal muscle fibers of the frog. *J. Gen. Physiol.* 120:349–368. http://dx.doi.org/10.1085/jgp.20028620

Berlin, J.R. 1995. Spatiotemporal changes of Ca^{2+} during electrically evoked contractions in atrial and ventricular cells. *Am. J. Physiol.* 269:H1165–H1170.

Blatter, L.A., J. Hüser, and E. Ríos. 1997. Sarcoplasmic reticulum Ca^{2+} release flux underlying Ca^{2+} sparks in cardiac muscle. *Proc. Natl. Acad. Sci. USA.* 94:4176–4181. http://dx.doi.org/10.1073/pnas.94.8.4176

Bridge, J.H., P.R. Ershler, and M.B. Cannell. 1999. Properties of Ca^{2+} sparks evoked by action potentials in mouse ventricular myocytes. *J. Physiol.* 518:469–478. http://dx.doi.org/10.1111/j.1469-7793.1999.0469p.x

Brochet, D.X., D. Yang, A. Di Maio, W.J. Lederer, C. Franzini-Armstrong, and H. Cheng. 2005. Ca^{2+} blinks: rapid nanoscopic

store calcium signaling. *Proc. Natl. Acad. Sci. USA.* 102:3099–3104. http://dx.doi.org/10.1073/pnas.0500059102

Brum, G., A. González, J. Rengifo, N. Shirokova, and E. Ríos. 2000. Fast imaging in two dimensions resolves extensive sources of Ca^{2+} sparks in frog skeletal muscle. *J. Physiol.* 528:419–433. http://dx.doi.org/10.1111/j.1469-7793.2000.00419.x

Cannell, M.B., and C.H. Kong. 2012. Local control in cardiac E-C coupling. *J. Mol. Cell. Cardiol.* 52:298–303. http://dx.doi.org/10.1016/j.yjmcc.2011.04.014

Cannell, M.B., and C. Soeller. 1999. Mechanisms underlying calcium sparks in cardiac muscle. *J. Gen. Physiol.* 113:373–376. http://dx.doi.org/10.1085/jgp.113.3.373

Chandler, W.K., S. Hollingworth, and S.M. Baylor. 2003. Simulation of calcium sparks in cut skeletal muscle fibers of the frog. *J. Gen. Physiol.* 121:311–324. http://dx.doi.org/10.1085/jgp.200308787

Cheng, H., and S.Q. Wang. 2002. Calcium signaling between sarcolemmal calcium channels and ryanodine receptors in heart cells. *Front. Biosci.* 7:d1867–d1878.

Cheng, H., W.J. Lederer, and M.B. Cannell. 1993. Calcium sparks: elementary events underlying excitation-contraction coupling in heart muscle. *Science.* 262:740–744. http://dx.doi.org/10.1126/science.8235594

Cheng, H., M.B. Cannell, and W.J. Lederer. 1994. Propagation of excitation-contraction coupling into ventricular myocytes. *Pflugers Arch.* 428:415–417. http://dx.doi.org/10.1007/BF00724526

Cheng, H., L.S. Song, N. Shirokova, A. González, E.G. Lakatta, E. Ríos, and M.D. Stern. 1999. Amplitude distribution of calcium sparks in confocal images: theory and studies with an automatic detection method. *Biophys. J.* 76:606–617. http://dx.doi.org/10.1016/S0006-3495(99)77229-2

Colquhoun, D., and A.G. Hawkes. 1983. The principles of the stochastic interaction of ion-channel mechanisms. *In* Single-Channel Recording. B. Sakmann and E. Neher, editors. Springer, New York. 135–175.

Copello, J.A., A.V. Zima, P.L. Diaz-Sylvester, M. Fill, and L.A. Blatter. 2007. Ca^{2+} entry-independent effects of L-type Ca^{2+} channel modulators on Ca^{2+} sparks in ventricular myocytes. *Am. J. Physiol. Cell Physiol.* 292:C2129–C2140. http://dx.doi.org/10.1152/ajpcell.00437.2006

Cordeiro, J.M., K.W. Spitzer, W.R. Giles, P.E. Ershler, M.B. Cannell, and J.H. Bridge. 2001. Location of the initiation site of calcium transients and sparks in rabbit heart Purkinje cells. *J. Physiol.* 531:301–314. http://dx.doi.org/10.1111/j.1469-7793.2001.0301i.x

Endo, M., M. Tanaka, and Y. Ogawa. 1970. Calcium induced release of calcium from the sarcoplasmic reticulum of skinned skeletal muscle fibres. *Nature.* 228:34–36. http://dx.doi.org/10.1038/228034a0

Fabiato, A., and F. Fabiato. 1978. Calcium-induced release of calcium from the sarcoplasmic reticulum of skinned cells from adult human, dog, cat, rabbit, rat, and frog hearts and from fetal and new-born rat ventricles. *Ann. NY Acad. Sci.* 307:491–522. http://dx.doi.org/10.1111/j.1749-6632.1978.tb41979.x

Franzini-Armstrong, C., and A.O. Jorgensen. 1994. Structure and development of E-C coupling units in skeletal muscle. *Annu. Rev. Physiol.* 56:509–534. http://dx.doi.org/10.1146/annurev.ph.56.030194.002453

Hayashi, T., M.E. Martone, Z. Yu, A. Thor, M. Doi, M.J. Holst, M.H. Ellisman, and M. Hoshijima. 2009. Three-dimensional electron microscopy reveals new details of membrane systems for Ca^{2+} signaling in the heart. *J. Cell Sci.* 122:1005–1013. http://dx.doi.org/10.1242/jcs.028175

Hüser, J., S.L. Lipsius, and L.A. Blatter. 1996. Calcium gradients during excitation-contraction coupling in cat atrial myocytes. *J. Physiol.* 494:641–651.

Izu, L.T., W.G. Wier, and C.W. Balke. 1998. Theoretical analysis of the Ca^{2+} spark amplitude distribution. *Biophys. J.* 75:1144–1162. http://dx.doi.org/10.1016/S0006-3495(98)74034-2

Izu, L.T., J.R. Mauban, C.W. Balke, and W.G. Wier. 2001. Large currents generate cardiac Ca^{2+} sparks. *Biophys. J.* 80:88–102. http://dx.doi.org/10.1016/S0006-3495(01)75997-8

Jiang, Y.H., M.G. Klein, and M.F. Schneider. 1999. Numerical simulation of Ca^{2+} "sparks" in skeletal muscle. *Biophys. J.* 77:2333–2357. http://dx.doi.org/10.1016/S0006-3495(99)77072-4

Kettlun, C., A. González, E. Ríos, and M. Fill. 2003. Unitary Ca^{2+} current through mammalian cardiac and amphibian skeletal muscle ryanodine receptor channels under near-physiological ionic conditions. *J. Gen. Physiol.* 122:407–417. http://dx.doi.org/10.1085/jgp.200308843

Kirsch, W.G., D. Uttenweiler, and R.H. Fink. 2001. Spark- and ember-like elementary Ca^{2+} release events in skinned fibres of adult mammalian skeletal muscle. *J. Physiol.* 537:379–389. http://dx.doi.org/10.1111/j.1469-7793.2001.00379.x

Klein, M.G., H. Cheng, L.F. Santana, Y.H. Jiang, W.J. Lederer, and M.F. Schneider. 1996. Two mechanisms of quantized calcium release in skeletal muscle. *Nature.* 379:455–458. http://dx.doi.org/10.1038/379455a0

Klein, M.G., A. Lacampagne, and M.F. Schneider. 1999. A repetitive mode of activation of discrete Ca^{2+} release events (Ca^{2+} sparks) in frog skeletal muscle fibres. *J. Physiol.* 515:391–411. http://dx.doi.org/10.1111/j.1469-7793.1999.391ac.x

Kockskämper, J., and L.A. Blatter. 2002. Subcellular Ca^{2+} alternans represents a novel mechanism for the generation of arrhythmogenic Ca^{2+} waves in cat atrial myocytes. *J. Physiol.* 545:65–79. http://dx.doi.org/10.1113/jphysiol.2002.025502

Kockskämper, J., K.A. Sheehan, D.J. Bare, S.L. Lipsius, G.A. Mignery, and L.A. Blatter. 2001. Activation and propagation of Ca(2+) release during excitation-contraction coupling in atrial myocytes. *Biophys. J.* 81:2590–2605. http://dx.doi.org/10.1016/S0006-3495(01)75903-6

Lacampagne, A., M.G. Klein, C.W. Ward, and M.F. Schneider. 2000. Two mechanisms for termination of individual Ca^{2+} sparks in skeletal muscle. *Proc. Natl. Acad. Sci. USA.* 97:7823–7828. http://dx.doi.org/10.1073/pnas.97.14.7823

Li, X., A.V. Zima, F. Sheikh, L.A. Blatter, and J. Chen. 2005. Endothelin-1-induced arrhythmogenic Ca^{2+} signaling is abolished in atrial myocytes of inositol-1,4,5-trisphosphate(IP_3)-receptor type 2-deficient mice. *Circ. Res.* 96:1274–1281. http://dx.doi.org/10.1161/01.RES.0000172556.05576.4c

Mackenzie, L., M.D. Bootman, M.J. Berridge, and P. Lipp. 2001. Predetermined recruitment of calcium release sites underlies excitation-contraction coupling in rat atrial myocytes. *J. Physiol.* 530:417–429. http://dx.doi.org/10.1111/j.1469-7793.2001.0417k.x

McCall, E., L. Li, H. Satoh, T.R. Shannon, L.A. Blatter, and D.M. Bers. 1996. Effects of FK-506 on contraction and Ca^{2+} transients in rat cardiac myocytes. *Circ. Res.* 79:1110–1121.

Melzer, W., E. Ríos, and M.F. Schneider. 1984. Time course of calcium release and removal in skeletal muscle fibers. *Biophys. J.* 45:637–641. http://dx.doi.org/10.1016/S0006-3495(84)84203-4

Nelson, M.T., H. Cheng, M. Rubart, L.F. Santana, A.D. Bonev, H.J. Knot, and W.J. Lederer. 1995. Relaxation of arterial smooth muscle by calcium sparks. *Science.* 270:633–637. http://dx.doi.org/10.1126/science.270.5236.633

Niggli, E., and N. Shirokova. 2007. A guide to sparkology: the taxonomy of elementary cellular Ca^{2+} signaling events. *Cell Calcium.* 42:379–387. http://dx.doi.org/10.1016/j.ceca.2007.02.010

Picht, E., A.V. Zima, T.R. Shannon, A.M. Duncan, L.A. Blatter, and D.M. Bers. 2011. Dynamic calcium movement inside cardiac sarcoplasmic reticulum during release. *Circ. Res.* 108:847–856. http://dx.doi.org/10.1161/CIRCRESAHA.111.240234

Pratusevich, V.R., and C.W. Balke. 1996. Factors shaping the confocal image of the calcium spark in cardiac muscle cells. *Biophys. J.* 71:2942–2957. http://dx.doi.org/10.1016/S0006-3495(96)79525-5

Qin, J., A.V. Zima, M. Porta, L.A. Blatter, and M. Fill. 2009. Trifluoperazine: a rynodine receptor agonist. *Pflugers Arch.* 458:643–651. http://dx.doi.org/10.1007/s00424-009-0658-y

Ríos, E., M.D. Stern, A. González, G. Pizarro, and N. Shirokova. 1999. Calcium release flux underlying Ca^{2+} sparks of frog skeletal muscle. *J. Gen. Physiol.* 114:31–48. http://dx.doi.org/10.1085/jgp.114.1.31

Ríos, E., N. Shirokova, W.G. Kirsch, G. Pizarro, M.D. Stern, H. Cheng, and A. González. 2001. A preferred amplitude of calcium sparks in skeletal muscle. *Biophys. J.* 80:169–183. http://dx.doi.org/10.1016/S0006-3495(01)76005-5

Ríos, E., J. Zhou, G. Brum, B.S. Launikonis, and M.D. Stern. 2008. Calcium-dependent inactivation terminates calcium release in skeletal muscle of amphibians. *J. Gen. Physiol.* 131:335–348. http://dx.doi.org/10.1085/jgp.200709870

Santiago, D.J., J.W. Curran, D.M. Bers, W.J. Lederer, M.D. Stern, E. Ríos, and T.R. Shannon. 2010. Ca sparks do not explain all ryanodine receptor-mediated SR Ca leak in mouse ventricular myocytes. *Biophys. J.* 98:2111–2120. http://dx.doi.org/10.1016/j.bpj.2010.01.042

Satoh, H., L.A. Blatter, and D.M. Bers. 1997. Effects of $[Ca^{2+}]_i$, SR Ca^{2+} load, and rest on Ca^{2+} spark frequency in ventricular myocytes. *Am. J. Physiol.* 272:H657–H668.

Sham, J.S., L.S. Song, Y. Chen, L.H. Deng, M.D. Stern, E.G. Lakatta, and H. Cheng. 1998. Termination of Ca2+ release by a local inactivation of ryanodine receptors in cardiac myocytes. *Proc. Natl. Acad. Sci. USA.* 95:15096–15101. http://dx.doi.org/10.1073/pnas.95.25.15096

Sheehan, K.A., and L.A. Blatter. 2003. Regulation of junctional and non-junctional sarcoplasmic reticulum calcium release in excitation-contraction coupling in cat atrial myocytes. *J. Physiol.* 546:119–135. http://dx.doi.org/10.1113/jphysiol.2002.026963

Sheehan, K.A., A.V. Zima, and L.A. Blatter. 2006. Regional differences in spontaneous Ca^{2+} spark activity and regulation in cat atrial myocytes. *J. Physiol.* 572:799–809.

Shen, J.X., S. Wang, L.S. Song, T. Han, and H. Cheng. 2004. Polymorphism of Ca^{2+} sparks evoked from in-focus Ca^{2+} release units in cardiac myocytes. *Biophys. J.* 86:182–190. http://dx.doi.org/10.1016/S0006-3495(04)74095-3

Shirokova, N., and E. Ríos. 1997. Small event Ca^{2+} release: a probable precursor of Ca^{2+} sparks in frog skeletal muscle. *J. Physiol.* 502:3–11. http://dx.doi.org/10.1111/j.1469-7793.1997.003bl.x

Shirokova, N., A. González, W.G. Kirsch, E. Ríos, G. Pizarro, M.D. Stern, and H. Cheng. 1999. Calcium sparks: release packets of uncertain origin and fundamental role. *J. Gen. Physiol.* 113:377–384. http://dx.doi.org/10.1085/jgp.113.3.377

Smith, G.D., J.E. Keizer, M.D. Stern, W.J. Lederer, and H. Cheng. 1998. A simple numerical model of calcium spark formation and detection in cardiac myocytes. *Biophys. J.* 75:15–32. http://dx.doi.org/10.1016/S0006-3495(98)77491-0

Sobie, E.A., and W.J. Lederer. 2012. Dynamic local changes in sarcoplasmic reticulum calcium: Physiological and pathophysiological roles. *J. Mol. Cell. Cardiol.* 52:304–311. http://dx.doi.org/10.1016/j.yjmcc.2011.06.024

Sobie, E.A., K.W. Dilly, J. dos Santos Cruz, W.J. Lederer, and M.S. Jafri. 2002. Termination of cardiac Ca(2+) sparks: an investigative mathematical model of calcium-induced calcium release. *Biophys. J.* 83:59–78. http://dx.doi.org/10.1016/S0006-3495(02)75149-7

Soeller, C., and M.B. Cannell. 1999. Examination of the transverse tubular system in living cardiac rat myocytes by 2-photon microscopy and digital image-processing techniques. *Circ. Res.* 84:266–275.

Soeller, C., and M.B. Cannell. 2002. Estimation of the sarcoplasmic reticulum Ca^{2+} release flux underlying Ca^{2+} sparks. *Biophys. J.* 82:2396–2414. http://dx.doi.org/10.1016/S0006-3495(02)75584-7

Soeller, C., and M.B. Cannell. 2004. Analysing cardiac excitation-contraction coupling with mathematical models of local control. *Prog. Biophys. Mol. Biol.* 85:141–162. http://dx.doi.org/10.1016/j.pbiomolbio.2003.12.006

Soeller, C., D. Crossman, R. Gilbert, and M.B. Cannell. 2007. Analysis of ryanodine receptor clusters in rat and human cardiac myocytes. *Proc. Natl. Acad. Sci. USA.* 104:14958–14963. http://dx.doi.org/10.1073/pnas.0703016104

Stern, M.D., G. Pizarro, and E. Ríos. 1997. Local control model of excitation–contraction coupling in skeletal muscle. *J. Gen. Physiol.* 110:415–440. http://dx.doi.org/10.1085/jgp.110.4.415

Stern, M.D., L.S. Song, H. Cheng, J.S. Sham, H.T. Yang, K.R. Boheler, and E. Ríos. 1999. Local control models of cardiac excitation–contraction coupling. A possible role for allosteric interactions between ryanodine receptors. *J. Gen. Physiol.* 113:469–489. http://dx.doi.org/10.1085/jgp.113.3.469

Toomre, D., and J.B. Pawley. 2006. Handbook of biological confocal microscopy. *In* Handbook of Biological Confocal Microscopy. J.B. Pawley, editor. Springer, New York. 231.

Tsugorka, A., E. Ríos, and L.A. Blatter. 1995. Imaging elementary events of calcium release in skeletal muscle cells. *Science.* 269:1723–1726. http://dx.doi.org/10.1126/science.7569901

Wang, S.Q., L.S. Song, E.G. Lakatta, and H. Cheng. 2001. Ca^{2+} signalling between single L-type Ca^{2+} channels and ryanodine receptors in heart cells. *Nature.* 410:592–596. http://dx.doi.org/10.1038/35069083

Wang, S.Q., L.S. Song, L. Xu, G. Meissner, E.G. Lakatta, E. Ríos, M.D. Stern, and H. Cheng. 2002. Thermodynamically irreversible gating of ryanodine receptors in situ revealed by stereotyped duration of release in Ca(2+) sparks. *Biophys. J.* 83:242–251. http://dx.doi.org/10.1016/S0006-3495(02)75165-5

Wang, S.Q., M.D. Stern, E. Ríos, and H. Cheng. 2004. The quantal nature of Ca^{2+} sparks and in situ operation of the ryanodine receptor array in cardiac cells. *Proc. Natl. Acad. Sci. USA.* 101:3979–3984. http://dx.doi.org/10.1073/pnas.0306157101

Woo, S.H., L. Cleemann, and M. Morad. 2002. Ca^{2+} current-gated focal and local Ca^{2+} release in rat atrial myocytes: evidence from rapid 2-D confocal imaging. *J. Physiol.* 543:439–453. http://dx.doi.org/10.1113/jphysiol.2002.024190

Wu, J.Y., J. Vereecke, E. Carmeliet, and S.L. Lipsius. 1991. Ionic currents activated during hyperpolarization of single right atrial myocytes from cat heart. *Circ. Res.* 68:1059–1069.

Zhou, J., G. Brum, A. Gonzalez, B.S. Launikonis, M.D. Stern, and E. Ríos. 2003. Ca^{2+} sparks and embers of mammalian muscle. Properties of the sources. *J. Gen. Physiol.* 122:95–114. http://dx.doi.org/10.1085/jgp.200308796

Zhou, J., G. Brum, A. González, B.S. Launikonis, M.D. Stern, and E. Ríos. 2005. Concerted vs. sequential. Two activation patterns of vast arrays of intracellular Ca^{2+} channels in muscle. *J. Gen. Physiol.* 126:301–309. http://dx.doi.org/10.1085/jgp.200509353

ZhuGe, R., K.E. Fogarty, R.A. Tuft, L.M. Lifshitz, K. Sayar, and J.V. Walsh Jr. 2000. Dynamics of signaling between Ca^{2+} sparks and Ca^{2+}-activated K^+ channels studied with a novel image-based method for direct intracellular measurement of ryanodine receptor Ca^{2+} current. *J. Gen. Physiol.* 116:845–864. http://dx.doi.org/10.1085/jgp.116.6.845

Zima, A.V., J. Kockskämper, R. Mejia-Alvarez, and L.A. Blatter. 2003. Pyruvate modulates cardiac sarcoplasmic reticulum Ca^{2+} release in rats via mitochondria-dependent and -independent mechanisms. *J. Physiol.* 550:765–783. http://dx.doi.org/10.1113/jphysiol.2003.040345

Zima, A.V., J.A. Copello, and L.A. Blatter. 2004. Effects of cytosolic NADH/NAD(+) levels on sarcoplasmic reticulum Ca(2+) release in permeabilized rat ventricular myocytes. *J. Physiol.* 555:727–741. http://dx.doi.org/10.1113/jphysiol.2003.055848

Zima, A.V., E. Picht, D.M. Bers, and L.A. Blatter. 2008a. Partial inhibition of sarcoplasmic reticulum Ca release evokes long-lasting Ca release events in ventricular myocytes: role of luminal Ca in termination of Ca release. *Biophys. J.* 94:1867–1879. http://dx.doi.org/10.1529/biophysj.107.114694

Zima, A.V., E. Picht, D.M. Bers, and L.A. Blatter. 2008b. Termination of cardiac Ca^{2+} sparks: role of intra-SR [Ca^{2+}], release flux, and intra-SR Ca^{2+} diffusion. *Circ. Res.* 103:e105–e115. http://dx.doi.org/10.1161/CIRCRESAHA.107.183236

Zima, A.V., E. Bovo, D.M. Bers, and L.A. Blatter. 2010. Ca^{2+} spark-dependent and -independent sarcoplasmic reticulum Ca^{2+} leak in normal and failing rabbit ventricular myocytes. *J. Physiol.* 588:4743–4757. http://dx.doi.org/10.1113/jphysiol.2010.197913